Rydberg exciton-polaritons in a Cu_2O microcavity

Konstantinos Orfanakis[1,+], Sai Kiran Rajendran[1,+], Valentin Walther[2,3], Thomas Volz[4,5], Thomas Pohl[6], and Hamid Ohadi[1,*]

[1]SUPA, School of Physics and Astronomy, University of St. Andrews, St. Andrews KY16 9SS, United Kingdom
[2]ITAMP, Harvard-Smithsonian Center for Astrophysics, Cambridge, MA, USA
[3]Department of Physics, Harvard University, Cambridge, MA, USA
[4]School of Mathematical and Physical Sciences, Macquarie University, Sydney, New South Wales, Australia
[5]ARC Centre of Excellence for Engineered Quantum Systems, Macquarie University, Sydney, New South Wales, Australia
[6]Center for Complex Quantum Systems, Department of Physics and Astronomy, Aarhus University, Aarhus, Denmark
[*]ho35@st-andrews.ac.uk
[+]these authors contributed equally to this work

ABSTRACT

Giant Rydberg excitons with principal quantum numbers as high as $n = 25$ have been observed in cuprous oxide (Cu_2O), a semiconductor where the exciton diameter can become as large as a micrometre. The giant dimension of these excitons results in excitonic interaction enhancements of orders of magnitude. Rydberg exciton-polaritons, formed by the strong coupling of Rydberg excitons to cavity photons, are a promising route to exploit these interactions and achieve a scalable, strongly correlated solid-state platform. However, the strong coupling of these excitons to cavity photons has remained elusive. Here, by embedding a thin Cu_2O crystal into a Fabry-Pérot microcavity, we achieve strong coupling of light to Cu_2O Rydberg excitons up to $n = 6$ and demonstrate the formation of Cu_2O Rydberg exciton-polaritons. These results pave the way towards realising strongly interacting exciton-polaritons and exploring strongly correlated phases of matter using light on a chip.

Exciton-polaritons in semiconductor microcavities[1–4] have emerged as versatile light-matter interfaces that lead to remarkable developments in fundamental science and technology[5], from the observation of high-temperature Bose-Einstein condensation[6–8] and topological states[9] to future applications for scalable quantum simulations[10] and polaritonic devices[11]. While experiments could exploit exciton-exciton interactions to demonstrate optical nonlinearities[12,13] and non-classical effects[14–17] at high light intensities, the realisation of strong and controllable interactions remains an important frontier that would bring applications into the quantum domain. High-lying excitonic Rydberg states offer such interactions, and in particular cuprous oxide (Cu_2O) has been identified as a well-suited material with giant Rydberg excitons as large as $\sim 1\mu$m[18] resulting in strong blockade effects[19]. Yet, harnessing these interactions for applications has remained a challenge due to the weak light-matter coupling in this material.

Highly excited Rydberg excitons are difficult to find due to the small Rydberg constant of most materials. Cu_2O with a large Rydberg constant of $\mathscr{R} = 97$ meV is a rare exception showing Rydberg states with record principal quantum numbers of $n = 30$[18,20]. In such highly excited states, excitons become very sensitive to external fields[21,22] and feature mutual interactions that can be enhanced by more than ten orders of magnitude over that of the ground state[19]. The lowest conduction band and the highest valence band in Cu_2O have the same parity, such that the direct dipole transition in Cu_2O is parity forbidden[23] and leads to a Rydberg series of long-lived P-state excitons. Based on the linewidths observed for Rydberg excitons up to $n = 25$[18], the lifetimes can be anticipated between 200-400 ps, an order of magnitude larger than excitons in GaAs quantum wells. The associated long coherence times[24] combined with the strong Rydberg-state interactions hold great promise for a broad range of applications[25,26]. The renewed interest in excitons of Cu_2O has led to a large number of studies, as detailed in recent review articles[27,28].

The enhanced coherence, however, comes at a significant cost as the forbidden dipole transition also implies a small oscillator strength and correspondingly weak coupling of light to Rydberg excitons in Cu_2O. Here, we solve this problem by embedding a natural Cu_2O crystal between two highly reflective distributed Bragg reflectors (see Fig. 1b). Our fabricated Cu_2O microcavity reaches the strong light-matter coupling regime for Rydberg excitons with up to $n = 6$. This, in turn, makes it possible to form Rydberg exciton-polaritons, which we demonstrate using transmission microscopy with high spectral and spatial resolution. The ability to generate exciton-polaritons in high-lying Rydberg states opens the door to exploring quantum many-body phenomena of interacting photons[29] and complex quantum states of light[30].

Optical resonators can enhance the light-matter coupling and hybridise photons and excitons in a semiconductor. This hybridisation results in the emergence of polaritons, which behave as quasiparticles that can be observed as distinct resonances in spectroscopic measurements. Strong coupling to excited exciton states generates so-called Rydberg polaritons that inherit the special properties of Rydberg excitons[18,19] as

demonstrated and exploited successfully with atomic systems in recent years[31,32]. The yellow series of P-state excitons in Cu_2O features a large number of such exciton states that give rise to a series of narrow absorption peaks (see Fig.1a). This Rydberg series overlaps with a broad absorption background that emerges above the energy of the 1S-ortho exciton and originates from the virtual population of blue excitons, which subsequently decay into an optical phonon and the 1S-ortho exciton[33]. It turns out that the interplay of these two absorption channels gives rise to characteristic polariton resonances that we can probe and analyse via cavity-transmission spectroscopy.

Results

Absorption spectrum of Cu_2O

To examine the optical properties of our Cu_2O crystal, we cut a mined Cu_2O crystal along the [111] crystallographic plane, mechanically polish and thin it to a few tens of microns (see Methods and Supplementary Information S1 for more details). The surface quality of the crystal after polishing is confirmed through bright and dark-field microscopy. The sample is placed between two CaF_2 windows and mounted gently on a cold finger in a cryostat, ensuring that the strain on the crystal due to the substrate is minimised as the crystal cools down to cryogenic temperatures. For optical excitation, we use a green-yellow light-emitting diode (LED) with a centre wavelength of 554 nm, as well as a spectrally filtered supercontinuum white-light laser (see Supplementary Information S2). The absorption spectrum at $T = 4$ K reveals Rydberg states up to $n = 12$ and the continuous absorption background discussed above (see Fig. 1a). The asymmetric Fano profile of the exciton resonances caused by this background[34] is clearly visible. The smaller number of observed exciton lines compared to previous measurements[18] is due to the resolution of our spectrometer, the broadband spectrum of our excitation source, the higher temperature of the crystal ($T = 4$ K) and crystal quality.

Fabry-Pérot microcavity

To achieve strong photon coupling to these excitons, we fabricate a planar Fabry-Pérot microcavity by placing a new crystal between highly reflective mirrors. Two distributed Bragg reflectors (DBRs) form the top and bottom mirrors, with 13 and 10 pairs of SiO_2/Ta_2O_5 layers (Fig. 1b). We can obtain the quality factor of our cavity by measuring the cavity-transmission linewidth at normal incidence away from any exciton resonance. The experiment yields a quality factor $Q \approx 1,700$ that is smaller than the predicted value $Q \approx 2300$, which does not include the inhomogeneous broadening due to local cavity thickness modulation caused by DBR deposition, polishing and, the wedged structure of the cavity. From the experimental free spectral range of ~ 6.6 meV, we estimate an active layer thickness of $\ell \sim 31\mu$m. Fig. 1c shows a bright-field reflectivity image of this thin layer before depositing the top DBR, confirming the successful integration of the mirror and a smooth millimetre-sized Cu_2O sample with micron-scale thickness.

Exciton-polariton dispersion

We analyse the coupling between the photons and Rydberg excitons by measuring the polaritonic energy dispersion as a function of the in-plane wavevector $k_\parallel$ of our microcavity using a Fourier space imaging setup (see Supplementary Information S2). The planar microcavity produces longitudinal confinement of the light at the resonant wavelength λ_c and corresponding frequency ω_c. For a single coupled longitudinal mode, the cavity photons, thus, acquire a quadratic dispersion $E \approx \hbar\omega_c + \hbar^2 k_\parallel^2/2m_{\text{cav}}$, akin to particles moving in the transverse plane of the cavity mirrors with an effective mass m_{cav}[35]. Due to the much larger mass of the excitons, the excitonic dispersion is virtually flat for relevant in-plane momenta $k_\parallel$, and may cross the photon mode at the exciton energy. At sufficiently strong light-matter coupling, this gives rise to an avoided crossing and two new modes (upper and lower exciton-polariton) that are separated by the vacuum Rabi splitting $\hbar\Omega_R$ (Fig. 2a). Our angle-resolved transmission spectrum reveals this exciton-photon hybridisation and demonstrates the formation of exciton-polaritons under strong coupling conditions for Rydberg states with $n = 3,\ldots,6$ (Fig. 2b). While the linewidth of the P-exciton ground state ($n = 2$) is too large to reach the strong coupling regime, the increasingly longer lifetime of the excited states makes it possible to form Rydberg polaritons under the conditions of our experiment in excellent agreement with the theoretical expectation based on transfer matrix calculations.

Asymmetric exciton-polariton dispersion

The large size of the sample makes it possible to scan the photon dispersion through the exciton resonance. To this end, we exploit the slightly wedged structure of the crystal after polishing ($\sim 0.6^\circ$). We vary the excitation position of the incident field to control the relevant thickness of the cavity, thereby tuning the energy of the cavity mode. By using a position scanner with a spatial resolution of 30 nm/step, the cavity transmission spectra can be scanned with high precision (~ 13 μeV/step), and reveal clear resonances as the cavity energy ($E_{\text{cav}} = \hbar\omega_c$) hits the exciton energies of the Rydberg series (E_n) (see Fig. 3). To determine the cavity-exciton detuning, $E_{\text{cav}} - E_n$, the nearest cavity mode needs to be identified for each Rydberg state. The cavity modes outside the yellow exciton transitions can be easily identified as they are far detuned from any excitons. From this, the cavity modes near the excitons can then be respectively calculated by a simple energy translation since the cavity modes are equally spaced in energy by $hc/(2\bar{n}\ell)$, where ℓ is the cavity thickness and $\bar{n}$ is the real refractive index of Cu_2O (see also Supplementary Information S3). A cavity mode comes into resonance with each Rydberg exciton transition as ℓ is scanned, and shows a clear splitting of the polariton modes for $n = 3,\ldots,6$.

Interestingly, the amplitude of the transmission peaks of the

upper and lower polaritons is not symmetric. This reflects the asymmetry of the exciton line, which originates from the continuous absorption background[18,34] discussed above, resulting in a Fano absorption profile $\alpha_n \propto \frac{\bar{\gamma}_n/2+2Q_n\Delta_n}{(\bar{\gamma}_n/2)^2+\Delta_n^2}$ with an asymmetry parameter $Q_n \neq 0$ and a transition linewidth $\bar{\gamma}_n$. Taking into account the underlying phonon-assisted absorption process, one can derive a simple expression for the resonant cavity transmission spectrum for the case when the cavity and a single exciton transition are resonant (see Methods for more details)

$$T_n \approx \frac{1}{\left(\frac{\tilde{\kappa}}{2}+G_n^2\frac{\bar{\gamma}_n/2+2Q_n\Delta_n}{(\bar{\gamma}_n/2)^2+\Delta_n^2}\right)^2+\left(\Delta_n-G_n^2\frac{\Delta_n-Q_n\bar{\gamma}_n}{(\bar{\gamma}_n/2)^2+\Delta_n^2}\right)^2}, \quad (1)$$

that gives transmission maxima at the expected polariton resonances as a function of the laser detuning $\Delta_n = \omega_{\mathrm{in}} - E_n/\hbar$. Here, $\tilde{\kappa}$ is the cavity linewidth far off-resonance, which includes losses from the phonon background. Equation 1 quantitatively explains the asymmetric transmission peaks observed in our experiments (see Fig. 4a). By fitting this expression to our measured resonant transmission spectra (see Supplementary Information S3), we can deduce the exciton-cavity coupling strength G_n. Considering that there is only one fitting parameter G_n and all other parameters in Eq. 1 are obtained from independent measurements (see Supplementary Table 1 for a full list of parameters), our theory yields remarkably good agreement with the measurements. From the theoretical line profiles, we can obtain the minimum value of G_n required to observe clearly separated polariton resonances (see Fig. 4b and also Supplementary Information S4). The depicted comparison to the measured values of G_n shows that our cavity just reaches the onset of the strong coupling regime for $n = 2$ and shows Rydberg polaritons well within the strong coupling regime for $n = 3,\ldots,6$.

Exciton-photon coupling strength

The photon coupling G_n decreases with n, reflecting the Rydberg scaling of the oscillator strength[18] (see Fig. 5), such that the strong-coupling condition is ultimately limited by the competition with the linewidth of the formed polaritons. The photon coupling can, in principle, be made stronger by increasing the cavity thickness, as a larger volume of the active medium collectively enhances the exciton-photon coupling. However, the phonon-induced absorption background in Cu_2O represents another photon-loss mechanism that adds to the linewidth of the cavity. Our transfer matrix calculations indicate that this competition leads to a finite ratio of the vacuum Rabi splitting to the linewidth of the polaritons as one increases the cavity-thickness (see Supplementary Information S5). Without the phonon absorption background, the calculations yield a steadily increasing ratio of the Rabi splitting to the polariton linewidth with increasing crystal thickness. With the phonon absorption background, the calculations also predict strong-coupling for all Rydberg states observed in the bulk crystal, but the coupling strength plateaus as cavity thickness increases (see Supplementary Information S5). The question then arises as to why in the experiment we are limited to $n = 6$ for strong coupling if we can observe states up to $n = 12$ in the bulk. This could be due to a few reasons: the plasma effect, the blockade effect, external strain or the charged defects in the crystal. The in-cavity intensity is sufficiently low that plasma effect[36] and the blockade effect can be neglected (see Supplementary Information S6). Our careful step-by-step spectroscopy during the fabrication process on a different sample shows that despite introducing some strain on our crystal, the effect is not significant enough to at least $n = 9$ (see Supplementary Information S7). We, therefore, believe that this particular crystal in our microcavity was not as high quality as that shown in Fig. 1.

Discussion

It is pertinent to compare our work to the current research on Rydberg exciton-polaritons in other materials. Recent work has achieved strong cavity coupling to excited exciton states in monolayers of WSe_2[37] and in a perovskite cavity containing single crystal $CsPbBr_3$ microplates[38] (see Supplementary Information S8 for a more detailed comparison). While all previous observations of exciton-polaritons have however been limited to $n = 2$, Cu_2O has the great advantage that narrow exciton lines with up to $n = 12$ can be routinely detected and now makes it possible to realise Rydberg polaritons with $n = 6$ in the presence of phonon coupling. Our calculations show that with experimentally feasible cavity thicknesses nonclassical light can already be observed for $n = 6$ polaritons (see Supplementary Information S6).

The phonon-induced absorption background can be eliminated via two-photon coupling to Rydberg S-state excitons[39], which will, thus, make it possible to achieve strong cavity coupling with even higher-lying Rydberg states. The demonstrated possibility to generate multiple excited levels in semiconductor microcavities will also permit the realisation of electromagnetically induced transparency, whereby a low-lying P-exciton can be strongly coupled to cavity photons and the transition to a highly excited S-state exciton is driven by an external control field[39,40]. Exploiting the strong van der Waals interaction between high-lying Cu_2O Rydberg-excitons[41], such Rydberg-EIT settings suggest exciting perspectives in combination with semiconductor microcavities. The results of our work thus present an essential step towards such new explorations of Rydberg polaritonics in the quantum regime.

With their greatly enhanced nonlinearities[19], induced by strong and long-range exciton interactions, Cu_2O Rydberg-exciton polaritons provide a versatile platform for exploring quantum many-body phenomena, extending the physics of weakly interacting photon fluids achievable with low-lying exciton states[5,16,42]. Previous measurements[18] suggest a blockade diameter of $\sim 0.5\mu$m for $n = 6$, and can reach values of $\sim 2\mu$m for $n = 10$. The associated polariton blockade under strong cavity-coupling thus offers a promising approach for

generating and manipulating non-classical states of light[43], whereby the use of synthetic Cu_2O micro-crystals[44–48], and micro-scale patterning[49,50] would yield configurable lattices of strongly interacting individual polaritons.

Acknowledgements

This work was supported by the EPSRC through grant No. EP/S014403/1, by The Royal Society through RGS\R2\192174, by the Carlsberg Foundation through the 'Semper Ardens' Research Project QCooL, by the NSF through a grant for ITAMP at Harvard University, by the DFG through the SPP1929, and by the Danish National Research Foundation through the Center of Excellence "CCQ" (Grant agreement no.: DNRF156). K.O. acknowledges EPSRC for PhD studentship support through grant no. EP/L015110/1. S.K.R. acknowledges the Carnegie Trust for the Universities of Scotland Research Incentive Grant RIG009823. T.V. acknowledges support through the Australian Research Council Centre of Excellence for Engineered Quantum Systems (CE170100009). V.W. acknowledges support by the NSF through a grant for the Institute for Theoretical Atomic, Molecular, and Optical Physics at Harvard University and the Smithsonian Astrophysical Observatory. We thank Jonathan Keeling for fruitful discussions. We also thank Yoshiko Nanao and EPSRC grant No. EP/T023449/1 for the XRD measurements.

Contributions

K.O. polished the sample, performed spectroscopy and analysed the data. S.K.R. deposited DBRs and performed the TMM simulations. V.W. and T.P. developed the theory. T.V. and H.O. supervised the project. H.O. conceived and designed the project. All authors contributed to the writing of the manuscript.

Competing interests

The authors declare no competing interests.

References

1. Weisbuch, C., Nishioka, M., Ishikawa, A. & Arakawa, Y. Observation of the coupled exciton-photon mode splitting in a semiconductor quantum microcavity. *Phys. Rev. Lett.* **69**, 3314–3317 (1992).
2. Lidzey, D. G. *et al.* Strong exciton–photon coupling in an organic semiconductor microcavity. *Nature* **395**, 53–55 (1998).
3. Dufferwiel, S. *et al.* Exciton-polaritons in van der Waals heterostructures embedded in tunable microcavities. *Nat. Commun.* **6**, 8579 (2015).
4. Fieramosca, A. *et al.* Two-dimensional hybrid perovskites sustaining strong polariton interactions at room temperature. *Sci. Adv.* **5**, eaav9967 (2019).
5. Carusotto, I. & Ciuti, C. Quantum fluids of light. *Rev. Mod. Phys.* **85**, 299–366 (2013).
6. Kasprzak, J. *et al.* Bose-Einstein condensation of exciton polaritons. *Nature* **443**, 409 (2006).
7. Plumhof, J. D., Stöferle, T., Mai, L., Scherf, U. & Mahrt, R. F. Room-temperature Bose–Einstein condensation of cavity exciton–polaritons in a polymer. *Nat. Mater.* **13**, 247–252 (2014).
8. Su, R. *et al.* Observation of exciton polariton condensation in a perovskite lattice at room temperature. *Nat. Phys.* **16**, 301–306 (2020).
9. Klembt, S. *et al.* Exciton-polariton topological insulator. *Nature* **562**, 552–556 (2018).
10. Amo, A. & Bloch, J. Exciton-polaritons in lattices: A non-linear photonic simulator. *Comptes Rendus Physique* **17**, 934–945 (2016).
11. Sanvitto, D. & Kéna-Cohen, S. The road towards polaritonic devices. *Nat. Mater.* **15**, 1061 (2016).
12. Ballarini, D. *et al.* All-optical polariton transistor. *Nat. Commun.* **4**, 1778 (2013).
13. Zasedatelev, A. V. *et al.* A room-temperature organic polariton transistor. *Nat. Photonics* **13**, 378–383.
14. Boulier, T. *et al.* Polariton-generated intensity squeezing in semiconductor micropillars. *Nat. Commun.* **5**, 3260 (2014).
15. Cuevas, A. *et al.* First observation of the quantized exciton-polariton field and effect of interactions on a single polariton. *Sci. Adv.* (2018).
16. Muñoz-Matutano, G. *et al.* Emergence of quantum correlations from interacting fibre-cavity polaritons. *Nat. Mater.* **18**, 213 (2019).
17. Delteil, A. *et al.* Towards polariton blockade of confined exciton–polaritons. *Nat. Mater.* **18**, 219–222 (2019).
18. Kazimierczuk, T., Fröhlich, D., Scheel, S., Stolz, H. & Bayer, M. Giant Rydberg excitons in the copper oxide Cu_2O. *Nature* **514**, 343–347 (2014).
19. Heckötter, J. *et al.* Asymmetric Rydberg blockade of giant excitons in Cuprous Oxide. *Nat. Commun.* **12**, 3556 (2021).
20. Versteegh, M. A. M. *et al.* Giant Rydberg excitons in Cu_2O probed by photoluminescence excitation spectroscopy. *Phys. Rev. B* **104**, 245206 (2021).
21. Thewes, J. *et al.* Observation of high angular momentum excitons in cuprous oxide. *Phys. Rev. Lett.* **115**, 027402 (2015).
22. Heckötter, J. *et al.* High-resolution study of the yellow excitons in Cu_2O subject to an electric field. *Phys. Rev. B* **95**, 035210 (2017).
23. Schweiner, F., Main, J., Feldmaier, M., Wunner, G. & Uihlein, C. Impact of the valence band structure of Cu_2O on excitonic spectra. *Phys. Rev. B* **93**, 195203 (2016).
24. Kitamura, T., Takahata, M. & Naka, N. Quantum number dependence of the photoluminescence broadening of excitonic Rydberg states in cuprous oxide. *J. Lumin.* **192**, 808–813 (2017).
25. Saffman, M., Walker, T. G. & Mølmer, K. Quantum information with Rydberg atoms. *Rev. Mod. Phys.* **82**, 2313–2363 (2010).
26. Weimer, H., Müller, M., Lesanovsky, I., Zoller, P. & Büchler, H. P. A Rydberg quantum simulator. *Nat. Phys.* **6**, 382–388 (2010).
27. Semina, M. A. Fine Structure of Rydberg Excitons in Cuprous Oxide. *Phys. Solid State* **60**, 1527–1536 (2018).
28. Aßmann, M. & Bayer, M. Semiconductor Rydberg physics. *Adv. Quantum Technol.* **3**, 1900134 (2020).
29. Hartmann, M. J. Quantum simulation with interacting photons. *J. Opt.* **18**, 104005 (2016).
30. Chang, D. E., Vuletić, V. & Lukin, M. D. Quantum nonlinear optics — photon by photon. *Nat. Photonics* **8**, 685–694 (2014).
31. Saffman, M., Walker, T. G. & Mølmer, K. Quantum information with Rydberg atoms. *Rev. Mod. Phys.* **82**, 2313–2363 (2010).
32. Browaeys, A. & Lahaye, T. Many-body physics with individually controlled Rydberg atoms. *Nat. Phys.* **16**, 132–142 (2020).
33. Schöne, F., Stolz, H. & Naka, N. Phonon-assisted absorption of excitons in Cu_2O. *Phys. Rev. B* **96**, 115207 (2017).
34. Toyozawa, Y. Interband effect of lattice vibrations in the exciton absorption spectra. *J. Phys. Chem. Solids* **25**, 59–71 (1964).
35. Kavokin, A. V., Baumberg, J. J., Malpuech, G. & Laussy, F. P. *Microcavities*. Series on Semiconductor Science and Technology (Oxford University Press, 2017).

36. Heckötter, J. *et al.* Rydberg excitons in the presence of an ultralow-density electron-hole plasma. *Phys. Rev. Lett.* **121**, 097401 (2018).

37. Gu, J. *et al.* Enhanced nonlinear interaction of polaritons via excitonic Rydberg states in monolayer WSe_2. *Nat. Commun.* **12**, 2269 (2021).

38. Bao, W. *et al.* Observation of Rydberg exciton polaritons and their condensate in a perovskite cavity. *Proc. Natl. Acad. Sci.* **116**, 20274–20279 (2019).

39. Walther, V., Grünwald, P. & Pohl, T. Controlling exciton-phonon interactions via electromagnetically induced transparency. *Phys. Rev. Lett.* **125**, 173601 (2020).

40. Walther, V., Johne, R. & Pohl, T. Giant optical nonlinearities from Rydberg excitons in semiconductor microcavities. *Nat. Commun.* **9**, 1309 (2018).

41. Walther, V., Krüger, S. O., Scheel, S. & Pohl, T. Interactions between Rydberg excitons in Cu_2O. *Phys. Rev. B* **98**, 165201 (2018).

42. Delteil, A. *et al.* Towards polariton blockade of confined exciton–polaritons. *Nat. Mater.* **18**, 219–222 (2019).

43. Gorshkov, A. V., Otterbach, J., Fleischhauer, M., Pohl, T. & Lukin, M. D. Photon-photon interactions via Rydberg blockade. *Phys. Rev. Lett.* **107**, 133602 (2011).

44. Lynch, S. A. *et al.* Rydberg excitons in synthetic cuprous oxide cu_2o. *Phys. Rev. Mater.* **5**, 084602 (2021).

45. Steinhauer, S. *et al.* Rydberg excitons in Cu_2O microcrystals grown on a silicon platform. *Commun. Mater.* **1**, 1–7 (2020).

46. Konzelmann, A., Frank, B. & Giessen, H. Quantum confined Rydberg excitons in reduced dimensions. *J. Phys. B: At. Mol. Opt. Phys.* **53**, 024001 (2019).

47. Ziemkiewicz, D., Karpiński, K., Czajkowski, G. & Zielińska-Raczyńska, S. Excitons in Cu_2O: From quantum dots to bulk crystals and additional boundary conditions for Rydberg exciton-polaritons. *Phys. Rev. B* **101**, 205202 (2020).

48. Orfanakis, K. *et al.* Quantum confined Rydberg excitons in Cu_2O nanoparticles. *Phys. Rev. B* **103**, 245426 (2021).

49. Jacqmin, T. *et al.* Direct observation of Dirac cones and a flatband in a honeycomb lattice for polaritons. *Phys. Rev. Lett.* **112**, 116402 (2014).

50. Ohadi, H. *et al.* Synchronization crossover of polariton condensates in weakly disordered lattices. *Phys. Rev. B* **97**, 195109 (2018).

Methods

Sample

Polishing and thinning—We start by cleaving a piece from a bulk natural Cu_2O crystal obtained from the Tsumeb mine in Namibia. It is essential that at least one surface of this piece is aligned with one of the crystallographic axes of the crystal, which is evidenced by a highly reflective, metallic-like, smooth surface. A fibre ferrule is then coated with a fast-acting adhesive soluble in ethanol. The sample is mounted on the ferrule with its natural facet side on top of the ferrule. This practice ensures that the sample will be aligned with one crystallographic axis after thinning. For thinning and polishing, we use lapping sheets of different grits (from 16 μm down to 0.3μm) commonly used for polishing fibres. The ferrule is mounted on a polishing puck which ensures that it is held perpendicular to the polishing paper. By moving the puck over the grit in a figure of eight, excess material from the crystal surface is removed. Every sample undergoes multiple polishing cycles, with inspection under a commercial microscope to ensure there are no features greater than the polishing grit. Once the polishing procedure is complete, we dissolve the glue with ethanol to separate the ferrule from the Cu_2O crystal. The sample is then placed on top of a DBR coated CaF_2 window with UV cured epoxy. After thinning the crystal down to $\sim 30\mu$m and polishing the second surface, the top DBR is deposited to form a cavity.

DBR coating —The bottom DBR consisting of 10 pairs of alternating 67.6 nm thick SiO_2 and 98.9 nm thick Ta_2O_5 was sputter deposited at room temperature on CaF_2 substrates to obtain maximum reflectivity at ~575 nm. The Cu_2O crystal was glued to the bottom DBR and a top DBR of 13 pairs of Ta_2O_5 and SiO_2 layers were then deposited directly on the Cu_2O crystal (see Supplementary Information S1).

Transfer matrix simulations

Using the experimental transmission spectra of Cu_2O at 4 K, the absorption coefficient $\alpha(\mathrm{cm}^{-1})$ of exciton transitions in Cu_2O was measured. The imaginary part of the refractive index (k) was obtained from the relation $\alpha(\lambda) = 4\pi k(\lambda)/\lambda$. The real part of the refractive index (n) was obtained from the Hilbert transform of k. The complex refractive index was then used in the transfer matrix method to obtain the transmission of light through the multi-layer DBR microcavity.

Theory

The absorption lines of the yellow series in Cu_2O show an asymmetric curve shape due to interference with a spectrally broad phonon-assisted background[33]. This affects the shape of the transmission resonances in a cavity, as shown below. In the excitation process, an incident photon can either excite any of the Rydberg exciton resonances n, described by $\hat{X}_n$, or a phonon-assisted continuum of states, described by $\hat{Y}$, both at center-of-mass momentum $\mathbf{k}$. The phonon-assisted states also have an internal (relative) momentum $\mathbf{k}'$. The coupling of the Rydberg excitons to the phonon background provides an interfering excitation pathway, thus creating a Fano resonance[51],

$$\begin{aligned}\partial_t \hat{X}_n(\mathbf{k}) =& -\frac{\Gamma_n}{2}\hat{X}_n(\mathbf{k}) - ig_n\mathscr{E}(\mathbf{k}) \\ & - i\sum_{\mathbf{k}'} h_{n,\mathbf{k},\mathbf{k}'}\hat{Y}(\mathbf{k},\mathbf{k}') \qquad (2)\\ \partial_t \hat{Y}(\mathbf{k},\mathbf{k}') =& -\frac{\Gamma_{\mathbf{k},\mathbf{k}'}}{2}\hat{Y}(\mathbf{k},\mathbf{k}') - ig^{\mathrm{bg}}_{\mathbf{k},\mathbf{k}'}\mathscr{E}(\mathbf{k}) \\ & - i\sum_{n} h_{n,\mathbf{k},\mathbf{k}'}\hat{X}_n(\mathbf{k}), \qquad (3)\end{aligned}$$

where $g^{\mathrm{bg}}_{\mathbf{k},\mathbf{k}'}$ denotes the optical coupling rate to the phononic states, $h_{n,\mathbf{k},\mathbf{k}'}$ the exciton-phonon coupling and $\Gamma_{\mathbf{k},\mathbf{k}'} = \gamma_{\mathbf{k},\mathbf{k}'} - 2i\Delta_{\mathbf{k},\mathbf{k}'}$ the complex phonon linewidth with linewidth $\gamma_{\mathbf{k},\mathbf{k}'}$ and detuning $\Delta_{\mathbf{k},\mathbf{k}'} = \omega_{\mathrm{in}} - \omega_{\mathbf{k},\mathbf{k}'}$. The variables associated with the Rydberg resonance are defined equivalently. The field $\mathscr{E}$ can be understood to give rise to a photon density $\langle\mathscr{E}^\dagger(\mathbf{k})\mathscr{E}(\mathbf{k})\rangle$ in mode $\mathbf{k}$. In the above description, we negect small contibutions from scattering processes involving multiple different phonons. In the steady state, we can solve for the continuum operators

$$\langle\hat{Y}(\mathbf{k},\mathbf{k}')\rangle = \frac{2}{\Gamma_{\mathbf{k},\mathbf{k}'}}\left[-ig^{\mathrm{bg}}_{\mathbf{k},\mathbf{k}'}\mathscr{E}(\mathbf{k}) - i\sum_n h_{n,\mathbf{k},\mathbf{k}'}\langle\hat{X}_n(\mathbf{k})\rangle\right]. \qquad (4)$$

The phonon states can be assumed as flat ($g^{\mathrm{bg}}_{\mathbf{k},\mathbf{k}'} = g^{\mathrm{bg}}_{\mathbf{k}}$ and $h_{n,\mathbf{k},\mathbf{k}'} = h_{n,\mathbf{k}}$) and dense in the relative momentum quantum number, allowing the sums to be evaluated

$$\begin{aligned}\sum_{\mathbf{k}'} h_{n,\mathbf{k},\mathbf{k}'}\langle\hat{Y}(\mathbf{k},\mathbf{k}')\rangle &\approx \left[-ih_{n,\mathbf{k}}g^{\mathrm{bg}}_{\mathbf{k}}\mathscr{E}(\mathbf{k}) - ih^2_{n,\mathbf{k}}\langle\hat{X}_n(\mathbf{k})\rangle\right]\tau_{\mathbf{k},n} \\ &= -i\bar{h}_{n,\mathbf{k}}\bar{g}^{\mathrm{bg}}_{n,\mathbf{k}}\mathscr{E}(\mathbf{k}) - i\bar{h}^2_{n,\mathbf{k}}\langle\hat{X}_n(\mathbf{k})\rangle, \qquad (5)\end{aligned}$$

where we defined $\tau_{\mathbf{k},n} \equiv \tau_{\mathbf{k}}(\omega_{\mathrm{in}} = \omega_n)$ from $\tau_{\mathbf{k}}(\omega_{\mathrm{in}}) = \sum_{\mathbf{k}'}\frac{2}{\Gamma_{\mathbf{k},\mathbf{k}'}}$ and absorbed it into $\bar{h}_{n,\mathbf{k}} \equiv \sqrt{\tau_{\mathbf{k},n}}h_{n,\mathbf{k}}$ and, similarly, $\bar{g}^{\mathrm{bg}}_{n,\mathbf{k}}$ (that have units $\sim\sqrt{\mathrm{energy}}$). We also neglected small contributions from off-resonant Rydberg states. While $\bar{h}_{n,\mathbf{k}}$ and $\bar{g}^{\mathrm{bg}}_{n,\mathbf{k}}$ can, in general, carry complex signatures of the underlying decay rates, we assume them here as real and constant across each exciton resonance. The polarisation, $\mathscr{P}(\mathbf{k}) = \chi_{\mathbf{k}}\mathscr{E}(\mathbf{k})$, can be solved explicitly and it defines $\chi_{\mathbf{k}}$ via

$$\begin{aligned}\mathscr{P}(\mathbf{k}) &= \sum_n g_n\langle\hat{X}_n(\mathbf{k})\rangle + \sum_{\mathbf{k}'} g^{\mathrm{bg}}_{\mathbf{k},\mathbf{k}'}\langle\hat{Y}(\mathbf{k},\mathbf{k}')\rangle \\ &= -i\sum_n \frac{(g_n - i\bar{g}^{\mathrm{bg}}_{n,\mathbf{k}}\bar{h}_{n,\mathbf{k}})^2}{\frac{\Gamma_n}{2} + \bar{h}^2_{n,\mathbf{k}}}\mathscr{E}(\mathbf{k}) - i(\bar{g}^{\mathrm{bg}}_{\mathbf{k}}(\omega_{\mathrm{in}}))^2\mathscr{E}(\mathbf{k}) \\ &= -i\sum_n g_n^2\frac{(1 - iQ_{n,\mathbf{k}})^2}{\frac{\bar{\gamma}_n}{2} - i\Delta_n}\mathscr{E}(\mathbf{k}) - i(\bar{g}^{\mathrm{bg}}_{\mathbf{k}}(\omega_{\mathrm{in}}))^2\mathscr{E}(\mathbf{k}), \qquad (6)\end{aligned}$$

where we introduced $\bar{\gamma}_n/2 = \gamma_n/2 + \bar{h}_n^2$ and the asymmetry parameter $Q_{n,\mathbf{k}} = \frac{\bar{g}^{\mathrm{bg}}_{n,\mathbf{k}} \bar{h}_{n,\mathbf{k}}}{g_n}$. The free-space absorption is

$$\alpha_{\mathbf{k}} = -\frac{2}{c\bar{n}} \Im(\chi_{\mathbf{k}}) = \sum_n \frac{4g_n^2}{c\bar{n}} \frac{\bar{\gamma}_n + 4Q_{n,\mathbf{k}}\Delta_n}{\bar{\gamma}_n^2 + 4\Delta_n^2} + \alpha_{\mathbf{k}}^{\mathrm{bg}}(\omega^{\mathrm{in}}) \tag{7}$$

with the refractive index $\bar{n}$ and where we dropped terms $\sim Q_{n,\mathbf{k}}^2$ under the assumption that $Q_{n,\mathbf{k}}^2 \ll 1$. We recognise a constant absorption term from the background as well as the plain exciton absorption if $Q_{n,\mathbf{k}} = 0$. The cross term originates from the interference between direct and indirect excitation of the background and produces an asymmetric lineshape. The standard in-cavity field equation for transverse momentum $\mathbf{k}_\perp$[5] is modified into

$$\partial_t \tilde{\mathscr{E}}(\mathbf{k}_\perp) = -\frac{\Gamma_{\mathrm{cav}}}{2} \tilde{\mathscr{E}}(\mathbf{k}_\perp) - \frac{i}{\bar{n}^2} \mathscr{P}(\mathbf{k}_\perp) + \eta_{\mathrm{in}} E^{\mathrm{in}}(\mathbf{k}_\perp) \tag{8}$$

with $\Gamma_{\mathrm{cav}} = \kappa - 2i(\omega_{\mathrm{in}} - (\omega_{\mathrm{cav}} + \hbar k_\perp^2/(2m_{\mathrm{ph}})))$, the cavity linewidth κ, the effective transverse photon mass m_{ph} and the external driving field E^{in} with corresponding coupling η. Transmission through the cavity at fixed $\mathbf{k}_\perp$ is proportional to the in-cavity intensity, $T = C_{\mathrm{out}}|\mathscr{E}|^2$, and is given by

$$T = \left[\left(\frac{\kappa}{2} + \sum_n \left(\frac{g_n}{\bar{n}}\right)^2 \frac{[1-Q_n^2]\frac{\bar{\gamma}_n}{2} + 2\Delta_n \cdot Q_n}{(\bar{\gamma}_n/2)^2 + \Delta_n^2} + \left(\frac{\bar{g}^{\mathrm{bg}}(\omega_{\mathrm{in}})}{\bar{n}}\right)^2 \right)^2 + \left(\Delta_{\mathrm{cav}} - \sum_n \left(\frac{g_n}{\bar{n}}\right)^2 \frac{[1-Q_n^2]\Delta_n - Q_n\bar{\gamma}_n}{(\bar{\gamma}/2)^2 + \Delta_n^2} \right)^2 \right]^{-1}. \tag{9}$$

We note that for comparison with Eq. (7), terms $\sim Q_n^2$ should be dropped, and $G_n = g_n/\bar{n}$ is the effective coupling strength.

Data availability

The research data underpinning this publication can be accessed from University of St Andrews Research Data repository at https://doi.org/10.17630/4f4e4d92-8309-45db-bade-26b147696138.

Methods References

51. Fano, U. Effects of configuration interaction on intensities and phase shifts. *Phys. Rev.* **124**, 1866–1878 (1961).

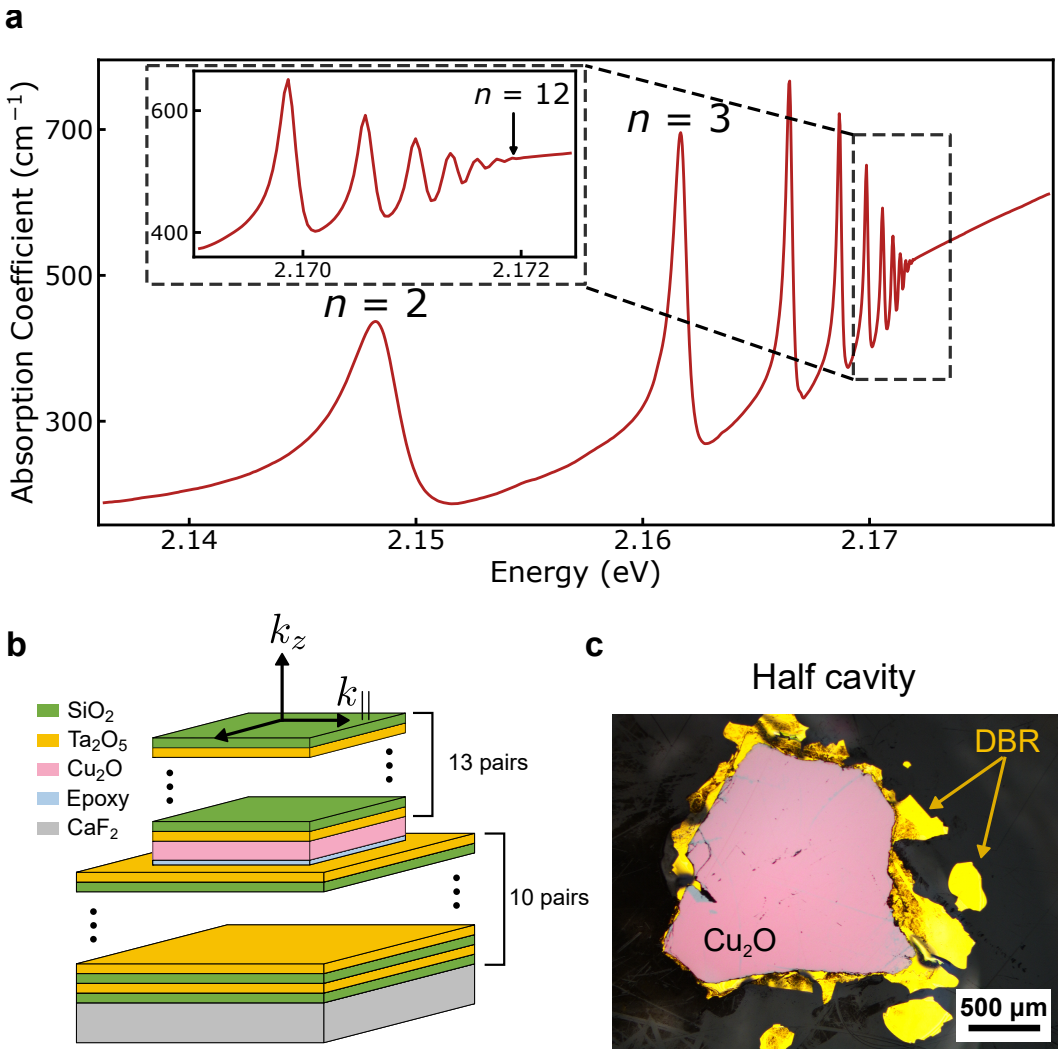

Figure 1. Absorption spectrum and cavity structure. a, Absorption coefficient α for a natural crystal of Cu_2O at 4 K measured in free space, where excitons up to $n = 12$ are resolved. The excitation source is a broadband LED (see Supplementary Information S2). Inset displays the higher energy region of the spectrum. **b**, Schematic illustration of the microcavity with the embedded Cu_2O crystal. **c**, Bright-field optical microscopy image of the half cavity. We note that the Cu_2O sample used in the cavity (**c**) is different from the one used for the absorption measurements (**a**).

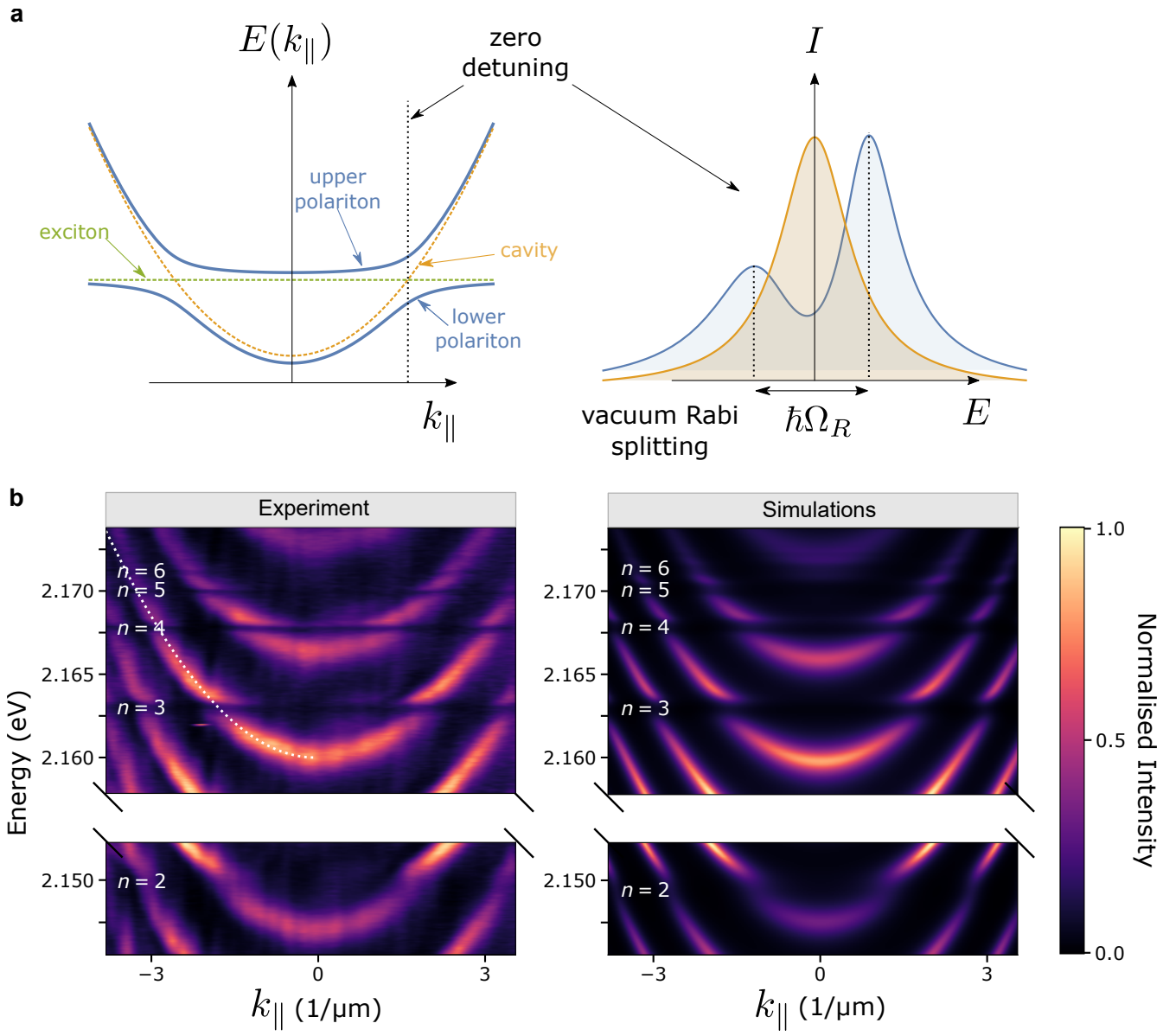

Figure 2. Momentum-space spectra. a, (left panel) The parabolic cavity dispersion (dotted orange) near an exciton transition (dotted green) modifies to an avoided crossing with two modes (upper and lower polariton, solid blue). Zero detuning (dotted line) is where the cavity and exciton modes cross. (right panel) The energy line profile at zero detuning (cavity resonant with exciton) shows a mode splitting equal to the vacuum Rabi splitting $\hbar\Omega_R$. **b**, Momentum-resolved transmission at 4 K from experiment (left) and TMM simulations (right). Dotted line shows the cavity mode. The excitation source in panel b is a top-hat resonant pulsed laser (see Supplementary Information S2).

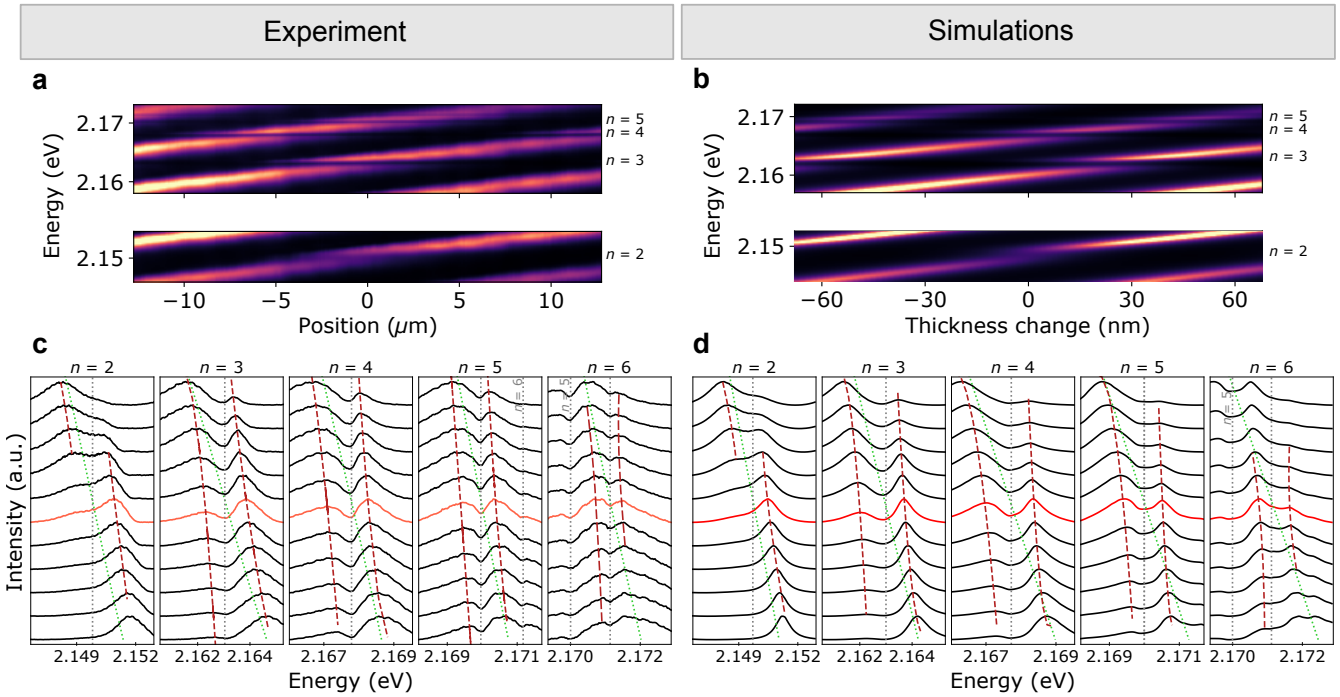

Figure 3. Real-space spectra. Experimental (**a**) and simulation (**b**) real-space spectra at $T = 4$ K at the vicinity of the first five P exciton states, and their intensity line profiles (**c,d**). Dotted lines represent the exciton (grey) and cavity modes (green). Dashed lines trace the upper and lower polariton branches. The orange lined spectrum is the line profile at zero detuning. The excitation source is a top-hat resonant pulsed laser (see Supplementary Information S2).

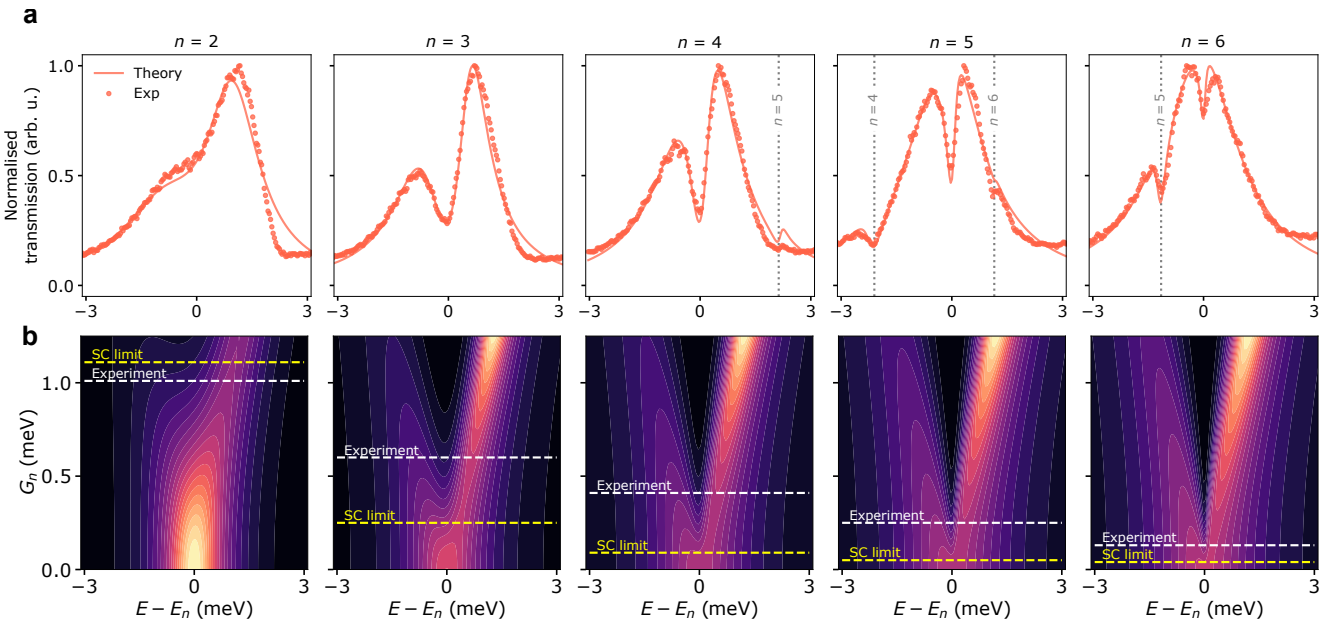

Figure 4. Zero-detuning line profiles and the effective coupling strength a, Experimental data and fitted lines for the lower and upper polariton branches at zero detuning (cavity resonant with exciton) for the $n = 2$, 3, 4, 5 and 6 exciton states. The excitation source in panel **a** is a top-hat resonant pulsed laser (see Supplementary Information S2). The small mismatch between the theory fits and the experiment at positive energies is due to the asymmetric cavity line profile (see Supplementary Information S3). **b**, Theoretical contour plots of the effective coupling strength, G_n, as a function of detuning for the $n = 2$, 3, 4, 5 and 6 exciton states. The strong coupling transition is depicted as yellow dashed line, while the experimentally obtained coupling strength is shown as a white dashed line.

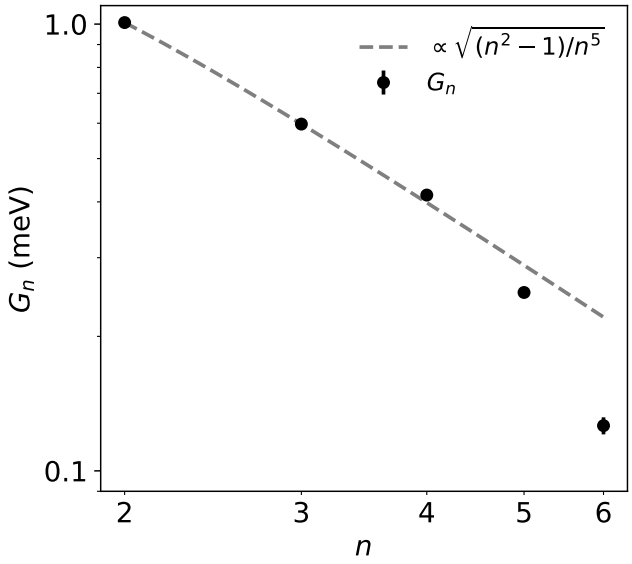

Figure 5. Scaling of coupling strength. Effective coupling strength parameter G_n vs quantum number n in the experiment (circles), and the square root of the theoretical oscillator strength (dashed line) show agreement with each other.

Supplemental Materials

S1 Sample

The distributed Bragg reflectors (DBRs) were fabricated by RF sputtering alternating layers of Ta_2O_5 and SiO_2 to obtain maximum reflectivity near 575 nm. The thicknesses of 100 nm Ta_2O_5 and SiO_2 layers deposited on microscope slides prior to DBR deposition were verified using ellipsometry and a correction to the tooling factor of the sputterer was performed to deposit layers of required thicknesses for the DBRs. There can be up to 5% variation in thickness depending on the position of the substrate in the chamber. The transmission spectra on co-deposited CaF_2 substrates were measured using an ellipsometer at normal incidence. There is good agreement between designed and experimentally characterised transmission spectra through the DBRs (see Fig. S1a) with a bandgap of 140 nm. The mismatch in the position of the bandgap is assigned to a difference in the obtained and expected thickness of layers deposited. The calculated transmittivity minima are 0.25 (0.27)% and 0.08 (0.03)% for 10 and 13 pair DBR respectively. This small mismatch is assigned to scattering losses in the substrates (60/40 scratch/dig) and mirrors when measured over a 2 mm spot diameter with an ellipsometer that can lead to a drop in the measured DBR transmission minimum and resultant quality factor by about 10%. The figure also shows the calculated transmission spectrum through a microcavity with a 32 μm thick transparent layer of refractive index 3, demonstrating the expected free spectral range and cavity linewidth of such a microcavity. The absorption coefficient of a 75 μm thick Cu_2O crystal measured with a large bandwidth low resolution (150 l/mm) grating is overlaid on the same figure to demonstrate the position of DBR bandgap and absorption of the P excitons.

The Cu_2O crystal was cut along the crystal planes of the natural crystal and mounted on a DBR coated CaF_2 window. After thinning and polishing the top surface, the top DBR is deposited to form a cavity (see Fig. S1b for bright field optical microscopy images of the front and back sides of the cavity). The cavity sample was then mounted on the sample stage in a Bruker D8 Discovery X-ray diffractometer. A $\theta - 2\theta$ scan was performed to extract the XRD spectrum of the Cu_2O crystal (Fig. S2). In the background, reference calculated XRD intensity and peak positions from a cubic Cu_2O crystal[52] are shown. It is clear that the Cu_2O crystal was cut and polished along the [111] crystal axis.

S2 Setup

The experimental setup is summarised in Fig. S3. For measuring the absorption spectrum of a bare Cu_2O crystal, the excitation source is a green-yellow light-emitting diode (LED) with a centre wavelength of 554 nm (Thorlabs MINTF4). For the real- and k-space spectroscopy of the microcavity, we use a broadband femtosecond white laser (NKT Laser SuperK EXTREME EXU-6) spectrally filtered by an acousto-optic modulator run at 10% amplitude to cover from 568 to 582 nm in wavelength (see Fig. S3b). The laser has a repetition rate of 78.1 MHz and ~5 ps pulse duration.

For absorption and real-space measurements, a plano-convex lens with $f = 25$ mm was used, creating an excitation spot ~ 3 μm. For the k-space measurements, an objective lens (Nikon 20×, NA = 0.40) focuses the excitation light to a spot ~ 1.5 μm. In all cases, an objective lens (Mitutoyo BD Plan Apo 20×, NA = 0.42) collects and collimates the transmitted light from our sample. The resulting signal is collected, dispersed and analysed in a spectrometer (Andor Shamrock 750) coupled to a cooled (Andor Newton) CCD camera. Samples are maintained at 4 K using a liquid-helium flow cryostat (Oxford Instruments MicrostatHe). We use CaF_2 substrates due to their excellent thermal conductivity at cryogenic temperatures and transparency in the visible spectrum.

S3 Fitting

It is critical to accurately determine the cavity-exciton detuning ($E_{cav} - E_{exc}$) for each n for our analysis. The first step involves determining the cavity modes in the vicinity of the exciton lines. Exciton absorption from multiple Rydberg exciton channels distorts the cavity modes, thus making it difficult to define them accurately. Therefore, we select the cavity mode at the low-energy side of our spectrum as it is the furthest away from the exciton lines. Owing to small thickness variations in our sample, the cavity modes cannot be described with straight lines. Consequently, the cavity mode is fitted with a 8^{th} degree polynomial (yellow line in Fig. S4).

Two cavity modes well away from the exciton transitions are identified and from that the spacing between adjacent modes is calculated. Since the cavity modes are equally spaced in energy, we then translate the fitted cavity line to find the modes in the vicinity of the first five exciton resonances (blue lines in Fig. S4). Zero detuning for each n can be accurately defined as the position where the exciton line intersects the corresponding cavity mode (green dashed lines in Fig. S4).

We fit the zero-detuning spectra to Eq. 9, which includes multiple exciton transitions. Including adjacent transitions is important for $n = 4 \ldots 6$ transitions, where the exciton energy spacing becomes comparable to the cavity linewidth. We fit Eq. 9 by varying parameters G_n and a normalising amplitude, while fixing other independently measured parameters such as $\tilde{\kappa}, Q_n$, and $\bar{\gamma}_n$.

The energy line profile of the resonance in a wedged planar Fabry-Perot cavity is asymmetric (see Ref.[53], Chapter 6). For the wedge angles such as in our sample (0.6 degree) the asymmetry is such that the high energy slope of the cavity is steeper than the low energy side. Fig. S5 shows a typical real-space spectrum near position zero of Fig. 3a. The off-resonant cavity mode shows a slight asymmetry (Fig. S5b) as well as broadening compared to the k-space line profile due to the larger spot size of real-space measurements (nearly twice due to the lower NA of the excitation lens).

S4 Minimum G_n for strong coupling

To determine the minimum value of G_n required to observe clearly separated polariton resonances, we start by using Eq. 1 to plot the theoretical transmission spectrum for a broad range of G_n values. For instance, for $n = 3$, we plot from $G_n = 0.1$ to 0.4, as shown in Fig. S6a.

A clear dip between the two polariton modes starts forming for a G_n value between 0.2 and 0.3. To accurately determine the exact value, we plot the derivative of the transmission spectrum for this range of values (see Fig. S6b). The minimum G_n is calculated as the first value where the derivative near resonance crosses zero (red dashed line in Fig. S6a). This corresponds to the case where the transmission flattens near the resonance. For $n = 3$, this is $G_n = 0.25$. For a greater G_n, there is a local minimum in the transmission function with two separate peaks on either side. We implement a similar routine for the other exciton transitions.

We define the strong coupling factor as the Rabi splitting divided by the polariton linewidth, and the system is in the strong coupling regime when there is a clear Rabi splitting present. Therefore, a nonzero strong coupling factor means the system is strongly coupled.

S5 Transfer matrix simulations

A key challenge towards calculating the coupling strength of Rydberg exciton transitions to the cavity mode was to obtain the correct optical response of Cu_2O. The clear presence of the yellow nP transitions can be observed only at cryogenic temperatures. Hence, the refractive index of Cu_2O ($\tilde{n} - ik$) must also be obtained at the same temperature, making it difficult to use standard techniques such as ellipsometry. By carefully recording the absorption coefficient of Cu_2O at 4 K, the imaginary part of the refractive index is obtained. The complex refractive index, following Kramers-Kronig relations, is then obtained using a Hilbert transformation of the imaginary part (see Fig. S7d). A constant real value of 3 was then added to the refractive index of Cu_2O in order to obtain a dispersion similar to that of the crystal[54]. The k values for Fig. S7b were obtained by extracting values from the optical response of Cu_2O in Ref. 33. This plot shows two broad absorption bands corresponding to the phonon-assisted absorption of the yellow $1S_y$ excitons for wavelengths shorter than 606 nm, and of the green $1S_g$ excitons for wavelengths shorter than 572 nm, respectively. When the phonon-assisted $1S_g$ component is removed, the optical response of only yellow P and $1S_y$ excitons remain (see Fig. S7c). When both the phonon-assisted absorption into $1S_y$ and $1S_g$ are removed, the optical response of only nP excitons can be extracted (Fig. S7a). Here, while k demonstrates the narrow nP resonances, there is a residual background absorption near the band edge that is assigned to the Urbach tail. The real parts of the corresponding refractive indices ($\tilde{n}$) are also shown in the same figures. These refractive indices can then be used to calculate the effect of such exciton transitions on the resultant polariton modes.

S5.1 Onset of strong coupling

The transfer matrix method (TMM) allows investigation into the strength of coupling between the yellow nP exciton transitions and the cavity mode. Using the estimated refractive index of Cu_2O ($\tilde{n} - ik$) the thickness of the crystal can be varied to tune the cavity mode into resonance with each of the exciton resonances, which takes place for thicknesses at integer multiples of $\lambda/2\tilde{n}$. The cavities in all TMM calculations consist of 13 and 10 pairs of alternating Ta_2O_5 and SiO_2 layers for the top and bottom DBRs as in the experiment.

Fig. S8 shows the transmitted dispersion spectra in a microcavity with different Cu_2O thicknesses. The energy of the P exciton transitions are plotted as dashed lines. For a $\lambda/2\tilde{n}$ cavity (crystal thickness of around 96 nm), while a broadening of the normal modes are observed when the cavity mode is in resonance with the exciton modes, no clear splitting is obtained. However, for a $21\lambda/2\tilde{n}$ cavity, clear splitting at $n = 3...7$ are visible, demonstrating strong coupling of the modes. For $n = 2$ transition, the strength of coupling to the cavity mode results in a broadening and splitting that are very close but a splitting smaller than the onset of strong coupling.

When detuning the cavity, the minima in normal mode splitting energy takes place when the cavity mode is in resonance with the exciton transition. The Rabi splitting energy is extracted and plotted in Fig. S9. The noise in the estimated Rabi splitting energy trend arises from the spectral resolution of 0.03 nm used to experimentally measure the absorption spectrum of Cu_2O crystal for TMM calculations. All P-exciton transitions show an increase in Rabi splitting energies with the increase in cavity thickness by integer multiples of $\lambda/2\tilde{n}$ due to the increase in absorption strength, and slowly saturate to a constant value. The highest splitting is obtained for the $n = 3$ transition, followed by the $n = 4$, 5 and 6 transitions. The increase in thickness of Cu_2O crystal required to observe the onset of strong coupling for increasing n is explained in the next section below.

S5.2 Phonon background on high n Rydberg strong coupling

To exploit the giant nonlinearity of Rydberg excitons, it is necessary to observe strong coupling in as high a principal quantum number n as possible. The reduction of oscillator strengths as well as spectral full widths at half maximum by the same scaling factor of n^{-3} would imply that transitions of all principal quantum numbers should be equally strongly coupled. In order to understand the origin of strong coupling in Cu_2O, we obtain TMM calculated Rabi splitting for exciton transitions when the Cu_2O optical response consists of only P excitons, as well as only when phonon-assisted 1S excitons are calculated. We find that the phonon-assisted 1S yellow and 1S green series excitons do not affect the Rabi splitting energy significantly but instead broaden the cavity mode. The Rabi splitting arises from the sharp yellow P exciton transitions.

The polariton linewidth depends on the averaged exciton and cavity linewidths weighted by their Hopfield coefficients.

Taking the polariton mode at resonance between the cavity mode with an exciton transition to consist of the superposition of just these two modes, the exciton and photonic components have equal magnitude and affect the polariton linewidth in equal weights. The polariton linewidths determine the lifetime of the polaritons, and the Rabi splitting energies determine the time period of oscillation between the hybrid states within those polariton lifetimes. The exciton linewidths fitted to the P exciton absorption spectra are shown in Fig. S10b. We extract the TMM calculated cavity linewidth by introducing two different optical responses. In a cavity with a transparent spacer, given by a constant refractive index of 3, the cavity spectral FWHM at wavelengths resonant with the nP exciton transitions shows an expected 1/thickness reduction (Fig. S10b) due to the increase of cavity round-trip time. In a cavity with phonon-assisted $1S_y$ and $1S_g$ transitions, with increasing active layer thickness, the cavity mode is broadened (Fig. S10a). It can be seen that all cavity modes present an increase in linewidth with an increase in crystal thickness as the resonant $1S_y$ absorption allows an additional decay channel for the photons. For cavity modes resonant with transitions of $n >= 5$, the modes are relatively broader due to additional absorption by the $1S_g$ excitons apart from the $1S_y$ excitons. A secondary broadening is also caused by the background Urbach tail resonant with high n Rydberg states. The former effect can be circumvented by two-photon absorption[39,40], first to a low lying S exciton followed by a transition to a higher P exciton.

When the Rabi splitting energy (Fig. S9) is divided by the corresponding polariton linewidth, we can define a strong coupling factor $\hbar\Omega/\gamma_{\rm pol}$. We are in the strong coupling regime when this factor is greater than zero. When the polariton linewidth obtained from a cavity mode broadened by the phonon-assisted transitions shown in Fig. S10a is used to calculate the coupling factor (i.e. when the phonon background is included in the absorption), the strong coupling factor $\hbar\Omega/\gamma_{\rm pol}$ plateaus quickly as the cavity thickness increases. (see Fig. S11a). This shows that the additional decay channel into the phonon-assisted $1S_g$ hinders the observation of strong coupling for high-n. However, if the polariton linewidth is calculated using values shown in Fig. S10b, where the P excitons can emit light only into the the cavity mode (i.e. when the phonon background is removed), the coupling factor increases as cavity thickness increases (see Fig. S11b). Hence it is clear that additional phonon-assisted absorption of the 1S excitons resonant with the P excitons is the main reason for the saturation of Rabi splitting with thickness, which poses a challenge towards the observation of strong coupling in high n giant Rydberg excitons. In our TMM simulations, we are also limited by estimation of Rabi splitting up to $n = 7$ due to the same limit on nP transitions observed in the absorption spectrum of our Cu_2O crystal sample. We note that this crystal sample was taken from the same batch of Cu_2O natural stone as that used in the cavity and hence a better comparison with our experimental spectra. On using the experimental absorption spectrum obtained from a different Cu_2O crystal as shown in Fig. 1a that shows clear resonance up to $n = 11$, TMM calculations were able to exhibit Rabi splitting up to $n = 11$. Hence Cu_2O presents potential for observation of high n strong coupling of ground state transitions. An alternative route to enhanced strong coupling and enhanced single-particle non-linearity may be achieved using EIT schemes[39,40]. However, the interaction strength of the $n = 3,\ldots,6$ p-exciton ground state transitions are sufficiently large to present an interesting opportunity to explore additional non-linearity induced when these polaritons interact with each other through cavity-mediated Rydberg blockade.

S6 Photon number and in-cavity intensity

The in-cavity photon number per cavity mode $n_{\rm cav}$ can be estimated from the spatially and wavelength-integrated CCD count rate ($R_{\rm 2D}$) of the transmission spectrum within a cavity mode energy range (e.g. see Fig. S5b). $R_{\rm 2D}$ is related to $n_{\rm cav}$ by:

$$R_{\rm 2D} = \frac{\beta_0 n_{\rm cav}}{\tau_{\rm RT}}\eta\,\tau_p \times {\rm PRF} \times \frac{\rm QE}{\alpha}, \tag{S1}$$

where $\beta_0 = 3\times10^{-4}$ is the measured transmission of the out-coupling DBR, $\tau_{\rm RT} \simeq 0.6$ ps is the cavity round-trip time, $\eta = 0.042$ is the total optical collection efficiency, $\tau_p = 5$ ps is the laser pulse duration, PRF = 78 MHz is the pulsed laser repetition frequency, QE = 0.97 is the CCD's quantum efficiency and $\alpha = 1.5\ e^-$/count is the CCD's sensitivity. Substituting $R_{\rm 2D} = 4.2\times10^6$ counts/s gives $n_{\rm cav} = 160\pm100$. We can estimate the peak in-cavity intensity $I_{\rm in-cavity-peak} = 2n_{\rm cav}h\nu/(\tau_{\rm RT}A) \simeq 26\ \mu{\rm W}/\mu{\rm m}^2$. Comparing this with the peak laser intensity incident on the sample ($I_{\rm laser-peak} \simeq 15$ mW/μm) gives a cavity throughput of $\sim 0.2\%$.

The blockade effect can result in non-classical light. The blockade effect arises from the competition of the interaction induced level shift and the width of the exciton line at a given principal quantum number n. For excitonic p-states, there are several potential curves with degenerate asymptotes that contribute to the nonlinearity. However, one can use the range of the resulting non-local nonlinear response (see, e.g. Ref. 36) to estimate the blockade radius. This yields a blockade radius of 1 μm at $n = 15$, as obtained from the measured nonlinear absorption without a cavity. This length scale is known to scale as $n^{7/3}$ with the principal quantum number n, such that one expects a blockade radius above 100 nm for $n = 6$.

The threshold particle number for non-linearity $n_{\rm th}$ is simply the mode volume of the cavity $V_{\rm cav}$ divided by the Rydberg volume ($4/3\pi r_{\rm Ry}^3$). Given the excitation spot diameter of 3 μm, cavity length $L = 31$ μm, the particle density for non-linearity in our cavity $n_{\rm th} \simeq 5\times10^4$, which is two orders of magnitude larger than our cavity photon number $n_{\rm cav}$. This, however, could be improved by reducing the thickness of the crystal and the spot size. For an experimentally achievable mode volume of 1 $\mu{\rm m}^3$, the cavity would saturate already at a level of $\sim$200 photons and generate non-classical light at

such low photon numbers for $n = 6$. It is therefore possible to reach the regime of a few strongly interacting polaritons for cavity-mode volumes achievable in our experiments.

S7 Strain effect in the sample

We record the photoluminescence (PL) spectrum at different cavity locations (see Fig. S12). The spectrum labelled 'Centre' (blue line in Fig. S12) corresponds to a location in the middle of the cavity sample and coincides with the area where Figs. 2-3 of the main text were recorded. The spectrum consists of the 1S ortho-exciton peak circa 609.6 nm and two broad features at ∼612.6 nm and ∼613.5 nm, corresponding to the ortho Γ_5^- and Γ_3^- excitons, respectively[57,58].

The 1S state is split by ∼67 pm. Applying strain along the [100] can cause the triply-degenerate 1S state to split into a singlet and a doublet with the singlet energy increasing and the doublet energy decreasing with strain[59,60]. The second spectrum, labelled 'Edge', corresponds to the spectrum with the highest observed splitting and was recorded at a location close to the edge of the cavity sample. In this case, the splitting is approximately double (∼135 pm) to that observed at the centre of the sample. In both cases, the observed splitting can be explained by a small amount of strain ($\ll 0.5$ kbar)[59,60].

The strain present in our cavity can be attributed to the fabrication process, namely glueing the Cu_2O sample to the substrate and depositing a DBR on top of it. To investigate the validity of this claim, we prepared a new Cu_2O sample and repeated the two fabrication steps mentioned above while optically characterising it before and after each step.

Following the procedure outlined in the Methods section, we thinned a new bulk Cu_2O crystal down to $\sim 30\ \mu$m. We then placed the new sample between two CaF_2 substrates and measured its absorption and PL spectra at 4 K (see blue lines in Fig. S13). We can reliably observe exciton peaks up to $n = 9$ in the absorption spectrum. The PL spectrum is dominated by the narrow (FWHM $\sim$ 0.04 nm) 1S ortho-exciton peak at ∼609.7 nm, accompanied by the Γ_5^- and Γ_3^- phonon-assisted peaks.

Subsequently, a thin layer of epoxy, similar to the one used for fabricating the cavity sample, was spin coated onto a new CaF_2 substrate, and the Cu_2O crystal was transferred onto the substrate and cured with UV light. The epoxy layer, after UV curing, has a thickness of $\sim 4\ \mu$m. We performed absorption and PL measurements on the same region of the crystal as before (orange lines in Fig. S13). The absorption spectrum reveals the same number of exciton resonances (up to $n = 9$), but there is a consistent blue shift of ∼0.2 nm for all peaks, compared to the sample sandwiched between the CaF_2 substrates. This shift could be due to better thermal contact between the crystal and the substrate in the presence of the optical glue. In the PL spectrum (orange line in Fig. S13b), the 1S ortho-exciton degeneracy is totally lifted, and the peak splits into three energy levels. This is consistent with strain applied across the [110] direction[61]. The splitting between the two extreme peaks is ∼1 nm (∼3 meV), which amounts to an applied strain of 1-1.5 kbar, i.e. significantly larger than the strain on our cavity.

The final step includes depositing a DBR on top of the bulk crystal mounted on the epoxy (black lines in Fig. S13). Here, we deposited a pair of SiO_2 and Ta_2O_5 layers, which is sufficient to reproduce any possible strain but is still transparent enough for transmission measurements. The absorption spectrum exhibits the same number of exciton transitions as the bare crystal before but is slightly blue shifted by only ∼0.01 nm compared to the glued sample, or equivalently, by ∼0.21 nm from the sample sandwiched between the CaF_2 substrates. A blue shift and triple splitting are present in the PL spectrum, similar to the glued sample.

Therefore, strain originating from the fabrication process is present, but it does not affect the number of exciton transitions present in the absorption spectrum. The question remains as to what the reason is for the reduced number of exciton transitions observed in the microcavity compared to that of the bulk. Given that our fabrication process is not causing the reduction of n, we believe that the number of exciton transitions in our cavity must be limited by the quality of our natural crystal sample. Even though all our samples originate from the same mother mineral stone, different parts can yield a slightly different number of exciton transitions due to the varying defect composition and internal stress from location to location.

S8 Comparison with other strongly coupled materials

Across different material systems for strong exciton-photon coupling, few works mention all four parameters: exciton linewidth, cavity linewidth, polariton linewidth and the Rabi splitting energy. A non-exhaustive list of strongly coupled materials and their parameters is presented in Table S2. Some of these parameters were extracted from other works in similar systems or estimated from other parameters such as Q factor or lifetime measurements as mentioned in the table caption.

Materials can be classified according to their range of exciton binding energies. Excitons of small binding energy are found in GaAs and CdTe. GaAs has a small exciton linewidth with a lifetime of 18 ps (see Fig. S14 for a comparison to Cu_2O). In early GaAs studies until the mid-2000s, the Q factors of GaAs cavities were only a few thousand. Around 2010, the number of pairs of layers in the DBRs was increased to report improved quality factors of values greater than 10,000, and in 2013 to 10^5 and 10^6. While such an improvement in cavity lifetimes did not increase the Rabi splitting energies, it allowed for better studies on polariton phenomena that took place within their transient lifetime. GaN and ZnO are large binding energy exciton systems and present a larger Rabi splitting energy as well as room temperature operation. For such materials, it is not essential to fabricate extremely high Q-factor cavities as the exciton linewidth is of the order of ∼100 meV. Organic semiconductors also possess large exciton binding energies enabling strong coupling at room temperatures.

Their exciton linewidths range from 10s of meV to ∼1 eV. While low Q factor metallic cavities or metal-DBR cavities are sufficient to observe strong coupling in such systems, DBR-DBR cavities are required for observation of polariton lasing or condensation. Two-dimensional van der Waals and perovskite materials also possess high exciton binding energies of a few 100 meV compared to their bulk counterparts. Both these materials are not suitable for top DBR fabrication and use bottom DBR-top metal cavity geometry, or a DBR-DBR open cavity system. The Rabi splitting energies obtained are in the same order of magnitude as their exciton linewidths. Strong coupling has also been demonstrated in a single molecule-plasmonic low-Q cavity. In summary, the limiting factor for the observation of strong exciton photon coupling seems to arise not from the cavity Q factor but the linewidths of the exciton transitions.

Comparing our system's parameters to the table below shows that the Cu_2O polariton system does not fully resemble any of the current materials. In terms of exciton linewidth, it is similar to high-quality GaAs quantum wells, the cavity linewidth is more like GaN microcavities, and the Rabi splitting resembles InGaAs systems. Comparing individual parameters, however, can be misleading as one should compare the ratios of the parameters or effectively the polariton spectra. If we compare the polariton spectra, our polariton spectra resemble those in the organics (porphyrin), the single-molecule plasmonic cavities, and the 2D materials.

Supplementary References

52. The Materials Project. Materials data on Cu_2O by Materials Project (2020).

53. Varu, H. *The optical modelling and design of Fabry Perot Interferometer sensors for ultrasound detection*. Ph.D. thesis, UCL (University College London) (2014).

54. Abu-Zeid, M. E., Rakhshani, A. E., Al-Jassar, A. A. & Youssef, Y. A. Determination of the thickness and refractive index of Cu_2O thin film using thermal and optical interferometry. *physica status solidi (a)* **93**, 613–620 (1986). URL https://onlinelibrary.wiley.com/doi/abs/10.1002/pssa.2210930226.

55. Walther, V., Johne, R. & Pohl, T. Giant optical nonlinearities from Rydberg excitons in semiconductor microcavities. *Nature Communications* **9**, 1309 (2018). URL https://doi.org/10.1038/s41467-018-03742-7.

56. Walther, V., Grünwald, P. & Pohl, T. Controlling exciton-phonon interactions via electromagnetically induced transparency. *Phys. Rev. Lett.* **125**, 173601 (2020). URL https://link.aps.org/doi/10.1103/PhysRevLett.125.173601.

57. Takahata, M. & Naka, N. Photoluminescence properties of the entire excitonic series in Cu_2O. *Physical Review B* **98**, 195205 (2018). URL https://link.aps.org/doi/10.1103/PhysRevB.98.195205.

58. Kang, D. D. *et al.* Temperature study of Rydberg exciton optical properties in Cu_2O. *Physical Review B* **103**, 205203 (2021). URL https://link.aps.org/doi/10.1103/PhysRevB.103.205203.

59. Waters, R. G., Pollak, F. H., Bruce, R. H. & Cummins, H. Z. Effects of uniaxial stress on excitons in Cu_2O. *Physical Review B* **21**, 1665–1675 (1980). URL https://link.aps.org/doi/10.1103/PhysRevB.21.1665.

60. Jang, J. I. & Wolfe, J. P. Relaxation of stress-split orthoexcitons in Cu_2O. *Physical Review B* **73**, 075207 (2006). URL https://link.aps.org/doi/10.1103/PhysRevB.73.075207.

61. Trebin, H. R., Cummins, H. Z. & Birman, J. L. Excitons in cuprous oxide under uniaxial stress. *Physical Review B* **23**, 597–606 (1981). URL https://link.aps.org/doi/10.1103/PhysRevB.23.597.

62. Kazimierczuk, T., Fröhlich, D., Scheel, S., Stolz, H. & Bayer, M. Giant Rydberg excitons in the copper oxide Cu_2O. *Nature* **514**, 343–347 (2014). URL https://www.nature.com/articles/nature13832.

63. Nelson, T. R. *et al.* Room-temperature normal-mode coupling in a semiconductor microcavity utilizing native-oxide AlAl/GaAs mirrors. *Applied Physics Letters* **69**, 3031–3033 (1996). URL http://aip.scitation.org/doi/10.1063/1.116829.

64. Wertz, E. *et al.* Spontaneous formation and optical manipulation of extended polariton condensates. *Nature Physics* **6**, 860–864 (2010). URL http://www.nature.com/articles/nphys1750.

65. Muñoz-Matutano, G. *et al.* Emergence of quantum correlations from interacting fibre-cavity polaritons. *Nature Materials* **18**, 213 (2019). URL https://www.nature.com/articles/s41563-019-0281-z.

66. Antoine-Vincent, N. *et al.* Observation of Rabi splitting in a bulk GaN microcavity grown on silicon. *Physical Review B* **68**, 153313 (2003). URL https://link.aps.org/doi/10.1103/PhysRevB.68.153313.

67. Butté, R. *et al.* Room-temperature polariton luminescence from a bulk GaN microcavity. *Physical Review B* **73**, 033315 (2006). URL https://link.aps.org/doi/10.1103/PhysRevB.73.033315.

68. Christopoulos, S. *et al.* Room-Temperature Polariton Lasing in Semiconductor Microcavities. *Physical Review Letters* **98**, 126405 (2007). URL https://link.aps.org/doi/10.1103/PhysRevLett.98.126405.

69. Lidzey, D. G. *et al.* Strong exciton–photon coupling in an organic semiconductor microcavity. *Nature* **395**, 53–55 (1998). URL http://www.nature.com/articles/25692.

70. Rajendran, S. K. *et al.* Low Threshold Polariton Lasing from a Solution-Processed Organic Semiconductor in a Planar Microcavity. *Advanced Optical Materials* **7**, 1801791 (2019). URL https://onlinelibrary.wiley.com/doi/10.1002/adom.201801791.

71. Dufferwiel, S. *et al.* Exciton-polaritons in van der Waals heterostructures embedded in tunable microcavities. *Nature Communications* **6**, 8579 (2015). URL http://www.nature.com/ncomms/2015/151008/ncomms9579/full/ncomms9579.html.

72. Gillard, D. J. *et al.* Strong exciton-photon coupling in large area $MoSe_2$ and WSe_2 heterostructures fabricated from two-dimensional materials grown by chemical vapor deposition. *2D Materials* **8**, 011002 (2021). URL https://iopscience.iop.org/article/10.1088/2053-1583/abc5a1.

73. Chikkaraddy, R. *et al.* Single-molecule strong coupling at room temperature in plasmonic nanocavities. *Nature* **535**, 127–130 (2016). URL http://www.nature.com/articles/nature17974.

74. Bouteyre, P. *et al.* Room-temperature cavity polaritons with 3D hybrid perovskite: toward large-surface polaritonic devices. *ACS Photonics* **6**, 1804 (2019). URL https://pubs.acs.org/doi/pdf/10.1021/acsphotonics.9b00625.

75. Bao, W. *et al.* Observation of Rydberg exciton polaritons and their condensate in a perovskite cavity. *Proceedings of the National Academy of Sciences* **116**, 20274–20279 (2019). URL http://www.pnas.org/lookup/doi/10.1073/pnas.1909948116.

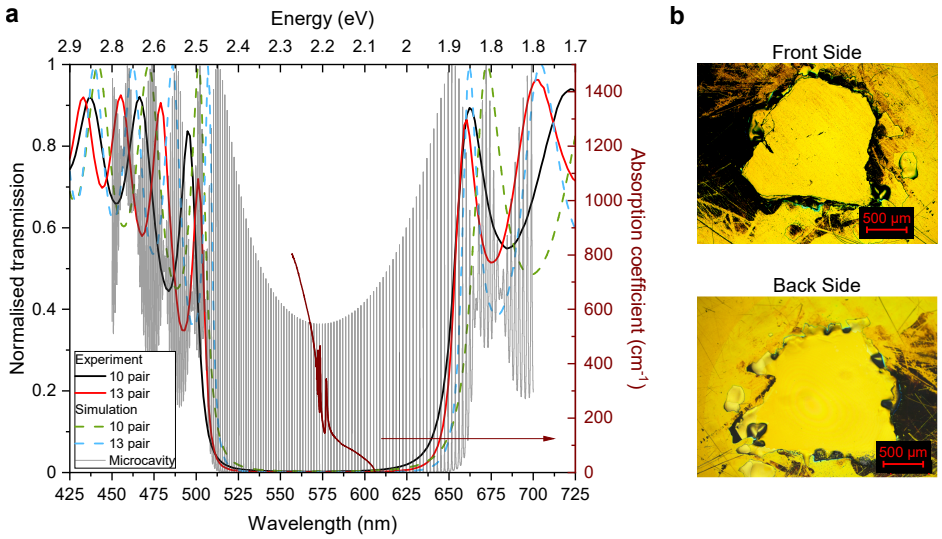

Figure S1. a, Transmission through the DBRs showing experimental (solid lines); and TMM simulated results for DBRs (dashed lines) and a cavity (grey solid line). An experimental absorption spectrum of a 75 μm thick Cu_2O crystal taken in a low spectral resolution broadband measurement (maroon solid line) is also overlaid. **b,** Bright-field optical microscopy images of the front (top panel) and back (bottom panel) sides of the cavity.

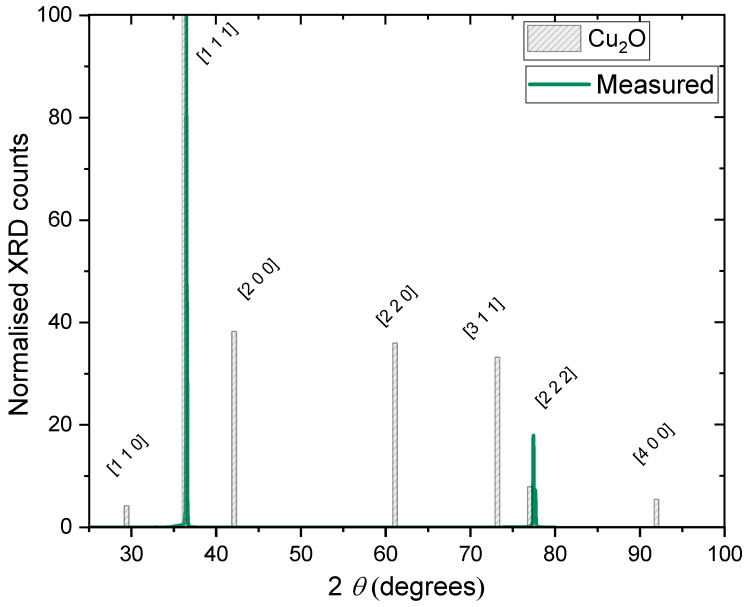

Figure S2. Experimental X-ray diffraction spectra of the Cu_2O crystal in the microcavity (green) overlaid on a calculated spectrum from cubic Cu_2O (grey).

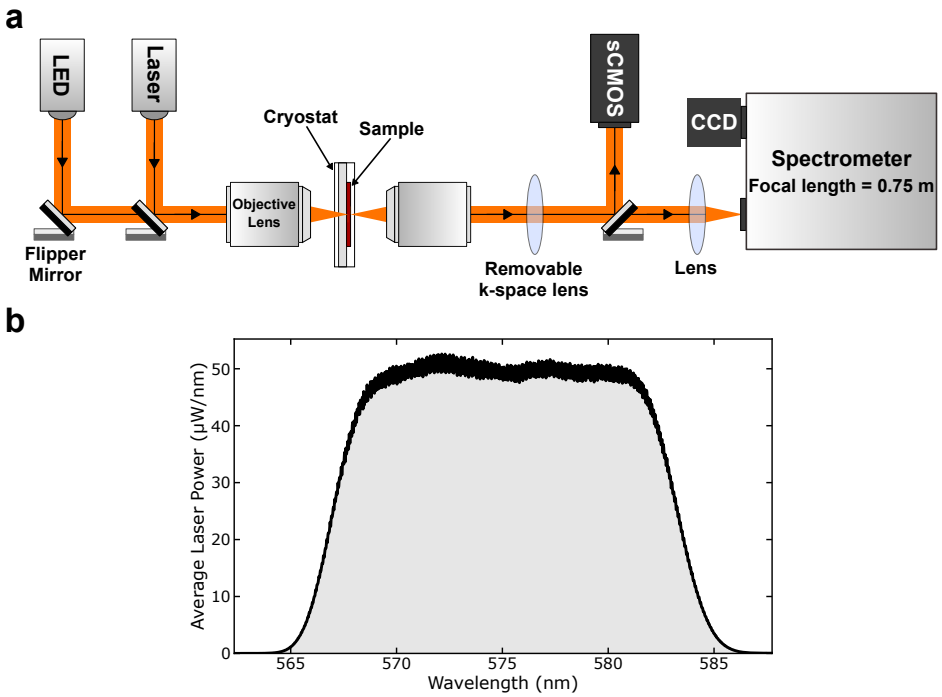

Figure S3. **a,** Schematic representation of our setup. **b,** Average power of our laser in μW/nm.

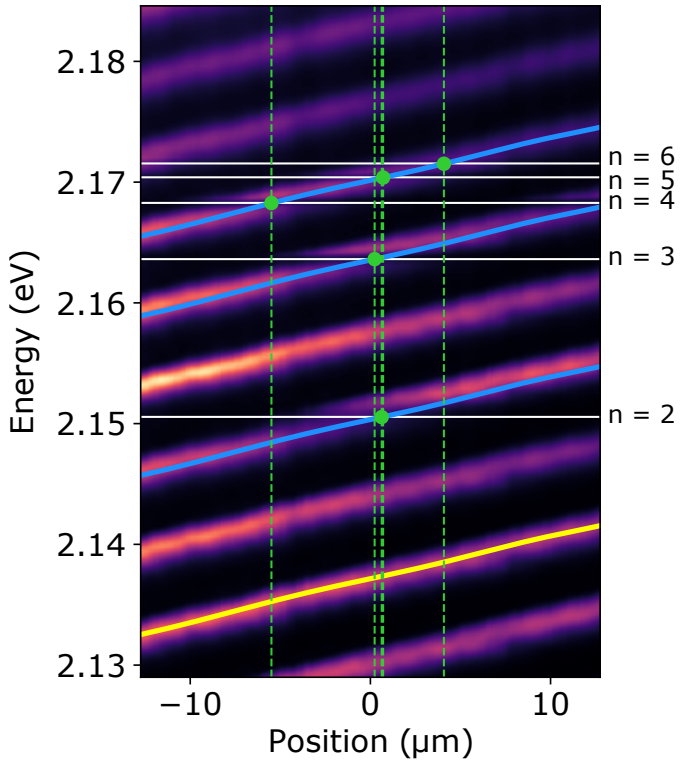

Figure S4. Experimental real-space spectrum at 4 K. Solid lines represent the exciton resonances (white) and cavity modes (blue and yellow). The point where each exciton line intersects with the corresponding cavity mode is denoted by a green dashed line.

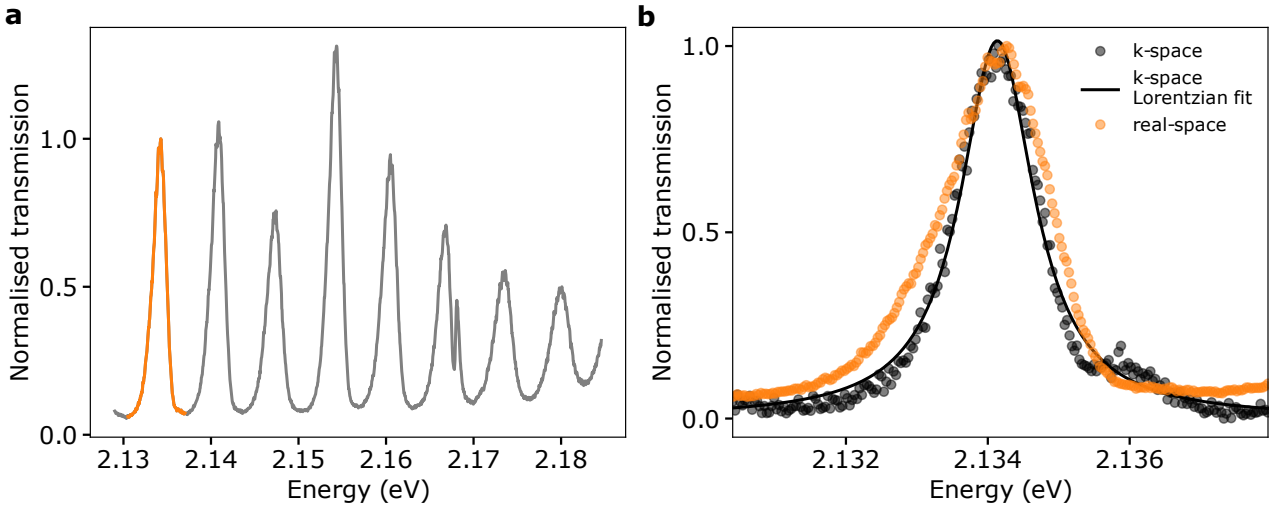

Figure S5. a, Energy line profile in Fig. S4 near zero detuning showing the off-resonant cavity line profile (highlighted in orange). **b,** Zoomed in cavity line profile in **a** showing the asymmetric lineshape broadening (FWHM $\sim$ 1.74 meV) due to the wedged structure of the cavity (orange circles). The line profile of the cavity from k-space measurement in Fig. 2 (black circles) and the Lorentzian fit (FWHM $\sim$ 1.26 meV).

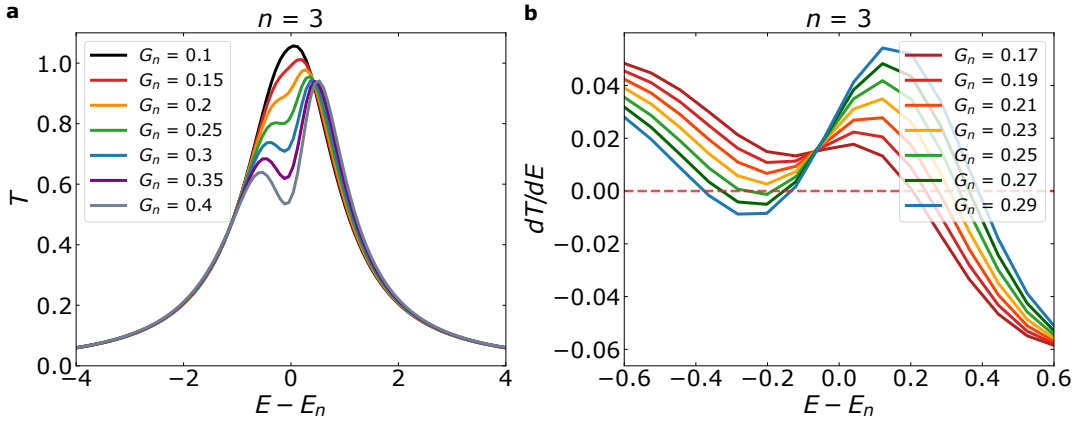

Figure S6. a, Theoretical transmission spectra for the $n = 3$ transition for different values of G_n. The spectra were calculated using Eq. 1. **b,** Derivative of the transmission spectra (dE/dT) with respect to energy for $n = 3$ for different values of G_n.

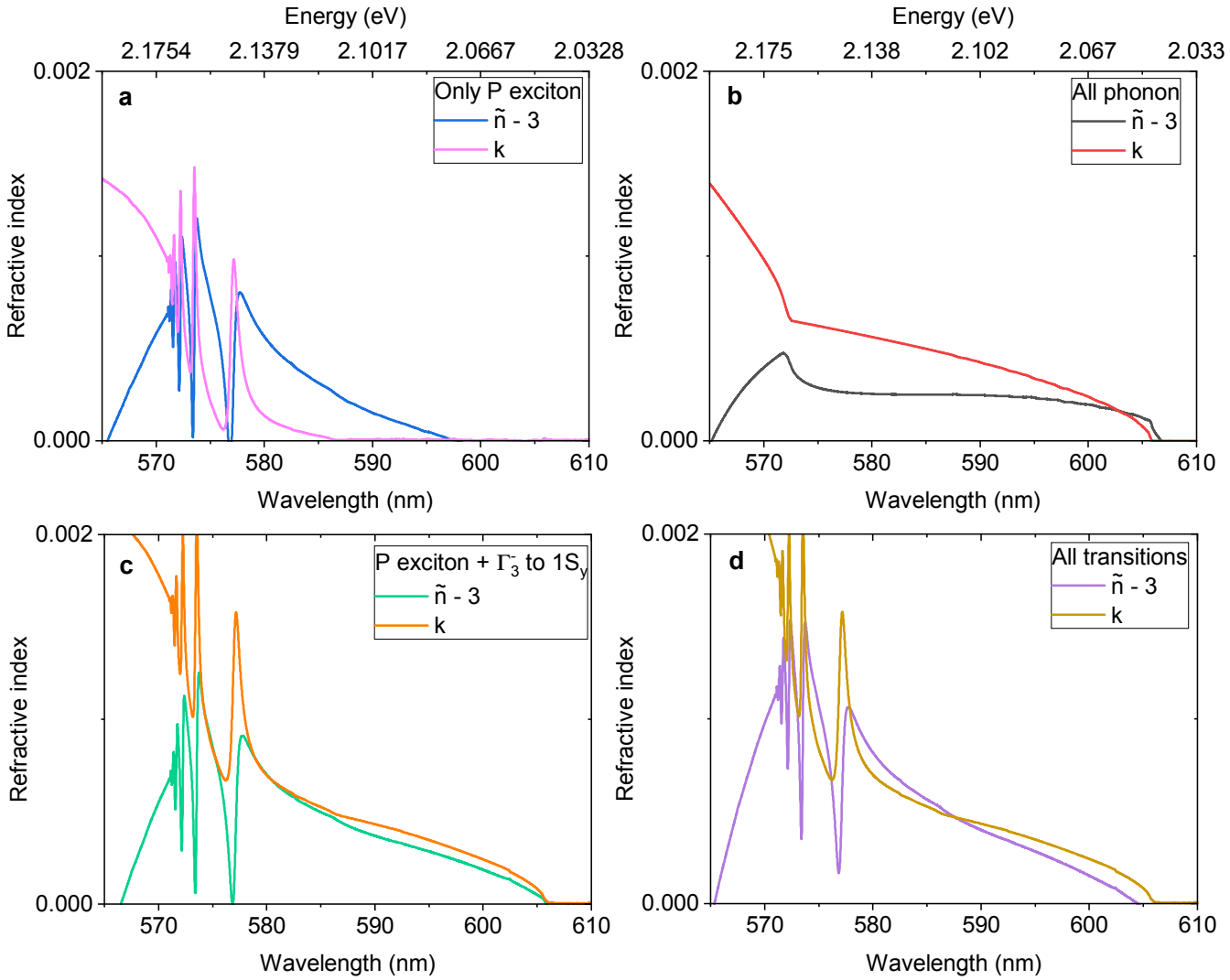

Figure S7. The complex refractive index of cuprous oxide at 4 K estimated when the absorption spectrum arises from **a,** P-excitons, **b,** only phonon-assisted 1S transitions, **c,** only yellow series excitons and **d,** all exciton transitions.

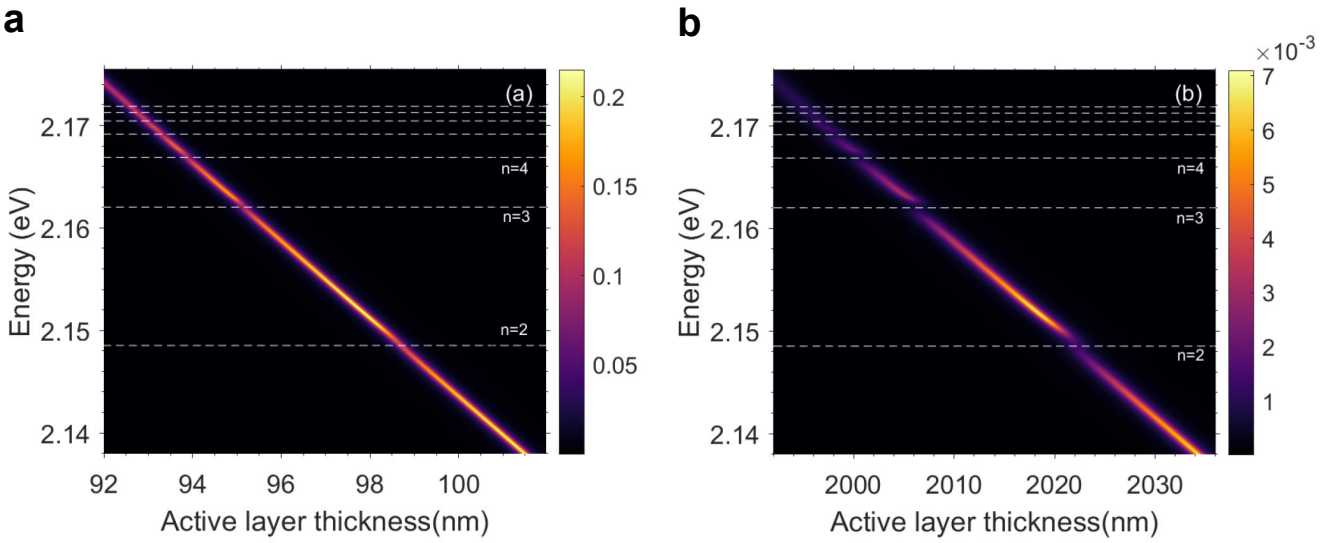

Figure S8. The calculated transmission through a microcavity with different cuprous oxide crystal thicknesses of **a,** $\lambda/2\tilde{n}$ and **b,** 21 $\lambda/2\tilde{n}$.

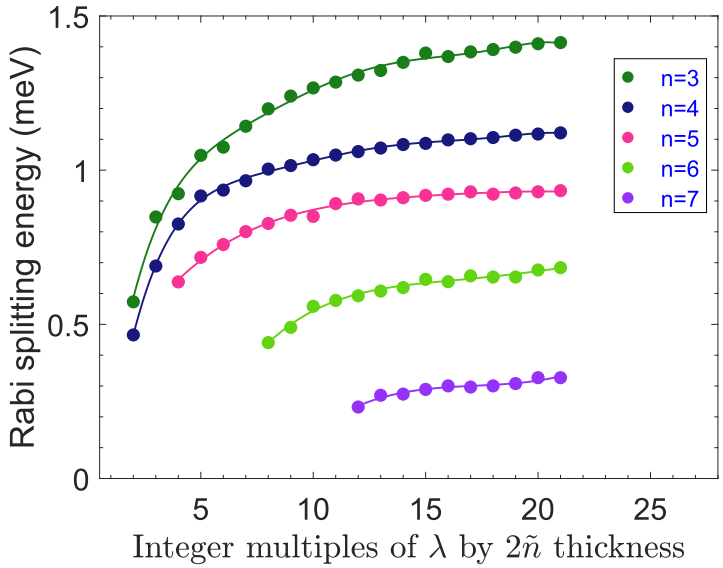

Figure S9. The calculated Rabi splitting energies of different cuprous oxide yellow transitions as a function of crystal thickness in the cavity.

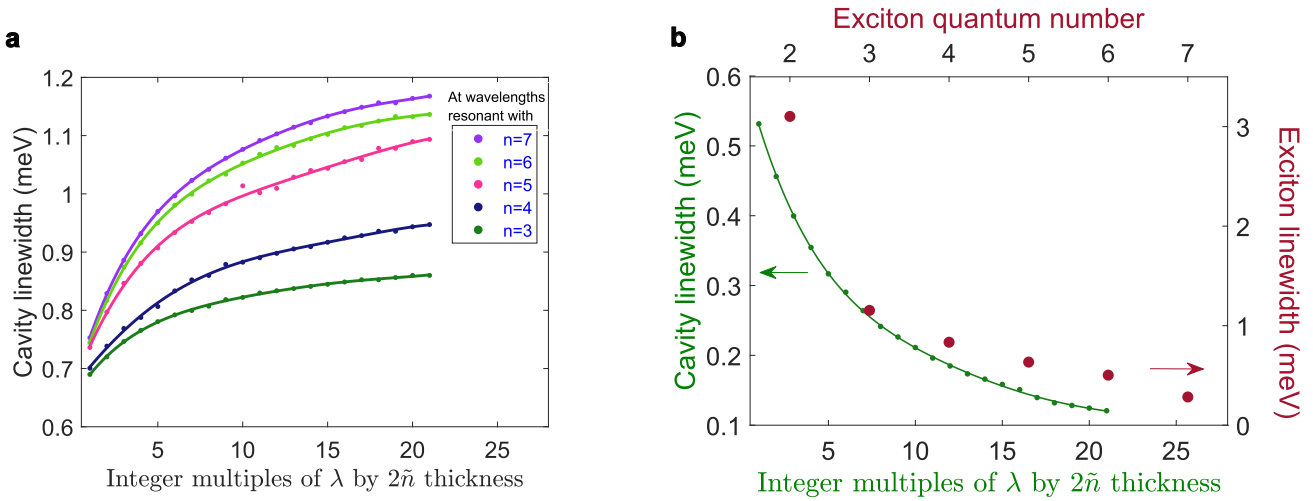

Figure S10. The extracted linewidths of the calculated cavity modes in the presence **a,** and absence **b,** of phonon-assisted transitions from TMM simulations. The P exciton linewidths are also shown as scatter plots (b).

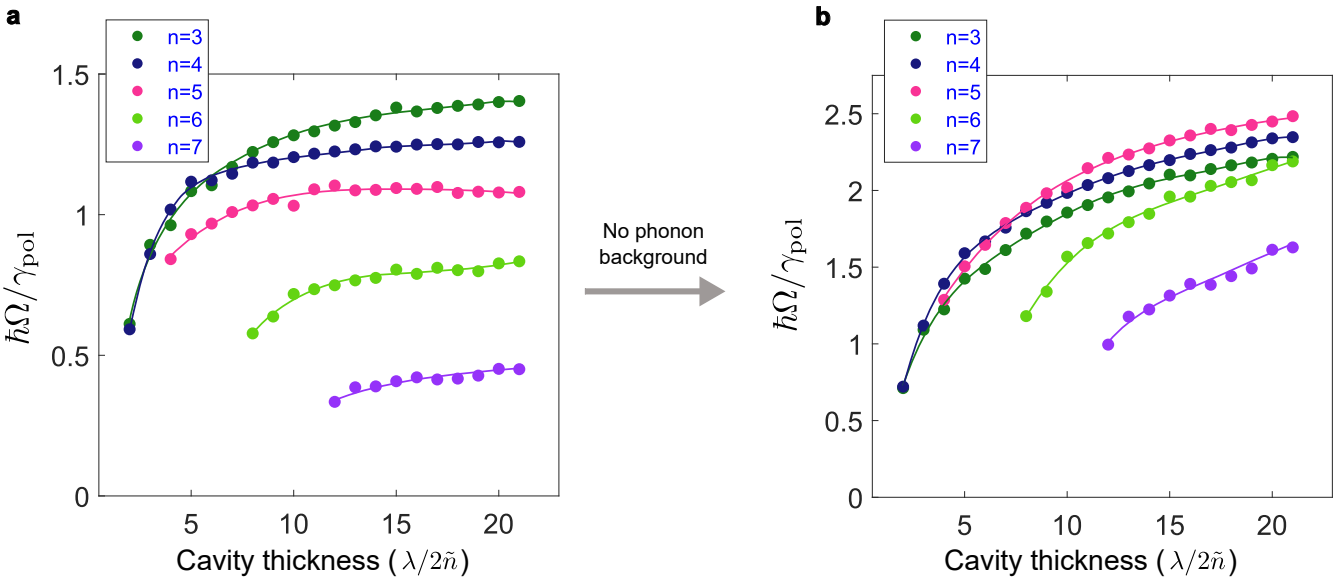

Figure S11. Transfer matrix calculations of the strong coupling factor ($\hbar\Omega/\gamma_{\mathrm{pol}}$) for the yellow P excitons **a,** in the presence and **b,** absence of phonon-assisted 1S transitions. The solid lines are a guide to the eye.

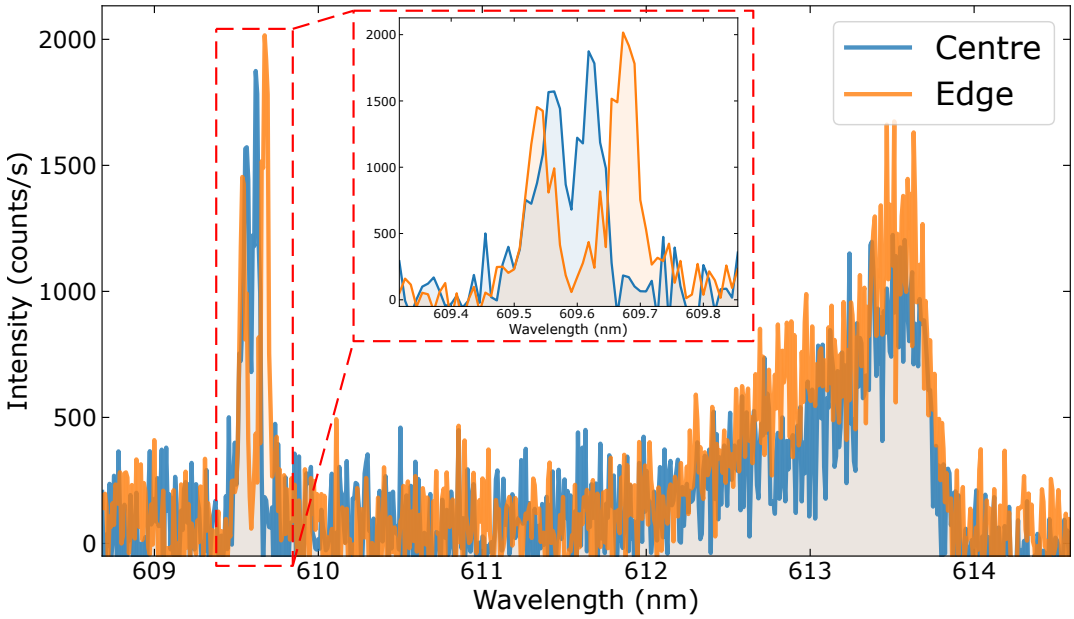

Figure S12. Photoluminescence spectra recorded from the centre (blue line) and from an edge of the cavity (orange line). Inset displays the spectral region around the 1S ortho-exciton.

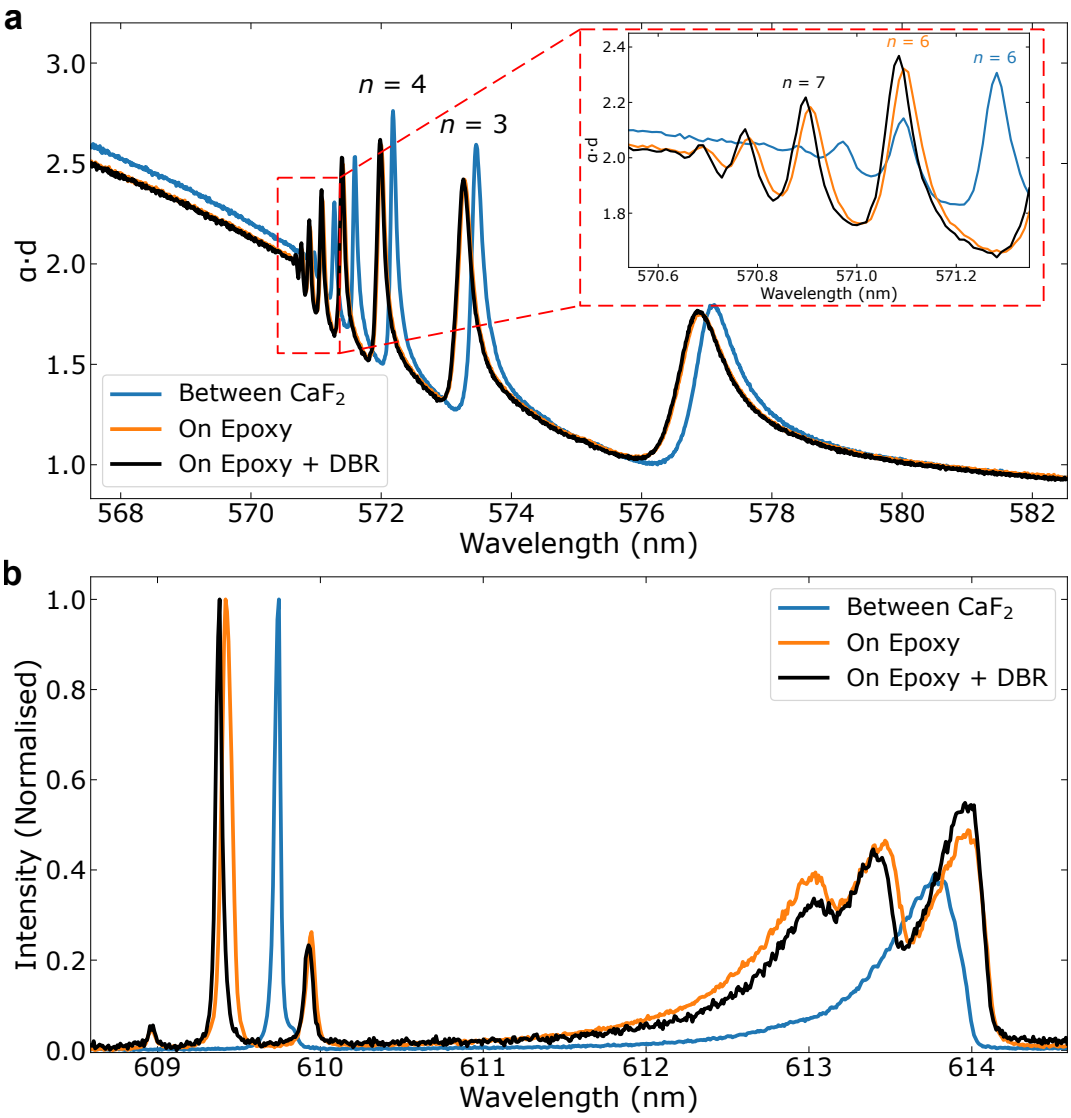

Figure S13. **a,** Absorption and **b,** PL spectra from a thin Cu_2O crystal between two transparent substrates (blue line), the same crystal mounted on a UV cured epoxy (orange line) and when a DBR is deposited on top of the crystal (black line).

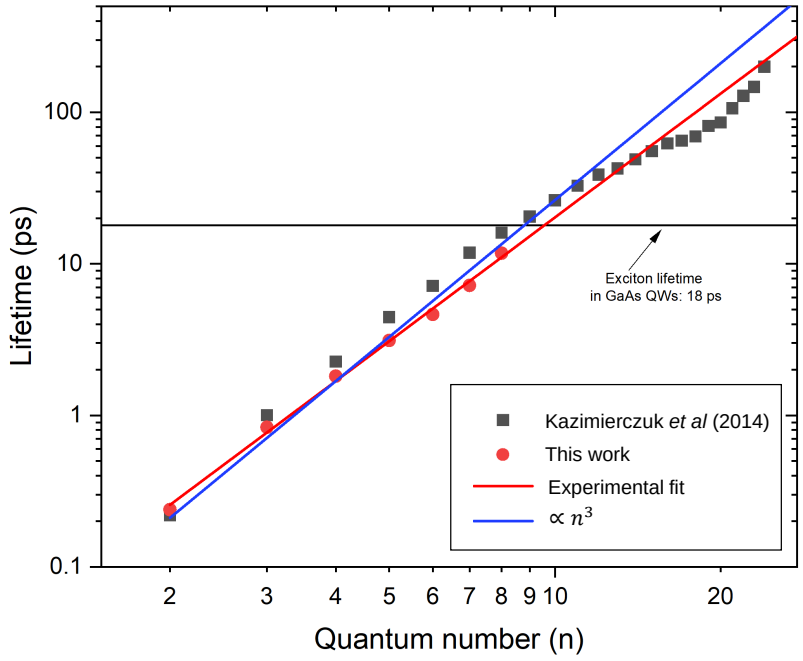

Figure S14. The lifetime of the P excitons is extracted from experimentally observed spectral full width at half-maximum from Ref.[18] (black scattered squares) and our own experimental spectra (red scattered circles). A fit to our experimental data (red line) is in reasonable agreement with the expected n^3 (black line) scalability in lifetime.

n	κ (meV)	γ (meV)	γ_{pol} (meV)	Q_n	$\hbar\Omega_R$ (meV)	$\hbar\Omega_R/\gamma_{\mathrm{pol}}$	min(G_n) for SC (meV)	G_n (meV)
2	1.44 ± 0.03	2.75 ± 0.02	2.09 ± 0.02	-0.251 ± 0.005	–	–	1.11 ± 0.01	1.01 ± 0.01
3	1.90 ± 0.03	0.789 ± 0.007	1.34 ± 0.02	-0.241 ± 0.005	1.50 ± 0.03	1.12 ± 0.03	0.25 ± 0.01	0.60 ± 0.01
4	2.37 ± 0.06	0.363 ± 0.005	1.36 ± 0.03	-0.212 ± 0.007	1.13 ± 0.03	0.83 ± 0.03	0.09 ± 0.01	0.41 ± 0.01
5	2.66 ± 0.05	0.211 ± 0.005	1.43 ± 0.03	-0.20 ± 0.01	0.89 ± 0.04	0.62 ± 0.03	0.05 ± 0.01	0.25 ± 0.01
6	2.64 ± 0.04	0.142 ± 0.005	1.39 ± 0.02	-0.17 ± 0.01	0.67 ± 0.04	0.48 ± 0.03	0.04 ± 0.01	0.13 ± 0.01

Table S1. Coupling parameters. Cavity linewidth κ, exciton linewidth γ, asymmetry parameter Q_n, vacuum Rabi splitting $\hbar\Omega_R$, minimum effective exciton-photon coupling G_n for strong coupling, and the fitted G_n at zero detuning for each Rydberg exciton transition n. γ_{pol} is the average exciton (γ) and cavity linewidth (κ). min(G_n) for strong coupling is theoretically calculated when two clear peaks in spectra are observed (that is when two local maxima are observed).

Material	Exciton linewidth κ (meV)	Cavity linewidth γ (meV)	Polariton linewidth γ_{pol} (meV)	Rabi splitting $\hbar\Omega_R$ (meV)
GaAs[63]	$0.036^{(a)}$	$0.0016^{(b)}$	$0.1^{(c)}$	13
GaAs[64]	$4^{(d)}$	$0.044^{(e)}$	$0.15^{(f)}$	15
InGaAs[16]	$0.066^{(g)}$	$0.05^{(h)}$	$0.044^{(i)}$	3
GaN[66–68]	$130^{(k)}$	$1.2^{(l)}$ $6^{(k)}$	$10^{(l)}$	31
Organics - Porphyrin[2]	90	$25^{(m)}$	20	110
Organics - Pentafluorene[70]	517	$10^{(o)}$	120	500
2D $MoSe_2$[3,72]	$1.6^{(p)}$ $13^{(q)}$		4.8 - 8.5	20 $17^{(q)}$
Single molecule - plasmonic cavity[73]	85	$120^{(r)}$	N.A.	380
Perovskite $CH_3NH_3PbBr_3$[74]	$90^{(s)}$	$25^{(s)}$	N.A.	70
Perovskite Rydberg $n = 2$ $CsPbBr_3$[38]	25		3	$37.4^{(t)}$ $29.6^{(u)}$

Table S2. Strong coupling in other systems. Experimental parameters for different materials in strongly coupled microcavities. Notes: (a) from exciton lifetime of 18 ps. (b) from photon lifetime of 400 ps, or designed Q factor of 10^6. (c) from instrumental spectral resolution of 7 ps, expected to be 100 ps lifetime. (d) from exciton photoluminescence spectra. (e) from 15 ps lifetime. (f) from polariton linewidth. (g) from exciton linewidth of 10 ps. (h) from Q factor of 30000. (i) from lower polariton lifetime of 15 ps, trions can have an additional effect. (k) at room temperature, Q factor of 800. (l) from Q factor of 2800. (m) from Q factors of 125. (o) linewidth at large negative detuning. (p) extracted from coupling strength, an exciton lifetime of 0.4 ps. (q) from [72]. (r) from Q factor 16. (s) from fitted parameters. (t) lower to middle polariton. (u) middle to upper polariton.